

The Pennsylvania State University

The Graduate School

**ULTRASONIC METHODS FOR CHARACTERIZATION OF ADDITIVELY  
MANUFACTURED MATERIALS: EXPERIMENTS AND NUMERICAL  
SIMULATIONS**

A Thesis in

Engineering Science & Mechanics

by

Colin L. Williams

© 2022 Colin L. Williams

Submitted in Partial Fulfillment  
of the Requirements  
for the Degree of

Master of Science

May 2022

The thesis of Colin L. Williams was reviewed and approved by the following:

Parisa Shokouhi  
Associate Professor of Engineering Science & Mechanics  
Thesis Co-Advisor

Matthew Lear  
Department Head, Structural Mechanics & Analysis, The Applied  
Research Laboratory at Penn State  
Assistant Research Professor of Engineering Science & Mechanics  
Thesis Co-Advisor

Jeremy M. Schreiber  
Assistant Research Professor, The Applied Research Laboratory at Penn  
State

Albert Segall  
Graduate Programs Officer  
Professor of Engineering Science and Mechanics

## ABSTRACT

The goal of this research is to find new noninvasive methods to certify the quality of safety-critical additively manufactured (AM) metallic parts for use in industries such as aerospace and defense. Additive manufacturing facilitates rapid prototyping, building, and repairing of custom components with increased agility, production rate, and reduced waste. A recognized barrier to the wide adoption of additive manufacturing is the lack of new approaches for AM part qualification. Our research objective is to exploit the material's linear and nonlinear ultrasonic response - which represents the measurable changes and distortion in elastic waves encountering macroscopic and microscopic defects - to establish links between microstructure and macroscale mechanical properties of AM metals.

We measure linear and nonlinear ultrasonic parameters for a series of AM and wrought 316L grade stainless steel samples and compare the obtained parameters against mechanical properties of the samples measured on corresponding coupons. The samples are heat-treated to different temperatures to induce microstructural changes which alter their mechanical properties and ultrasonic response. Two sets of specimens are manufactured, one from the additive manufacturing method Laser Powder Bed Fusion (L-PBF), and the second from a traditional wrought method. Using the nonlinear ultrasonic method of Second Harmonic Generation (SHG), the acoustic nonlinearity parameter is estimated. SHG has been shown to offer a highly sensitive response to microstructural heterogeneities such as dislocations and grain boundaries. A linear ultrasonic parameter, wave speed, is also recorded with pulse-echo testing. Alongside these ultrasonic measurements, mechanical testing parameters including elastic moduli and yield strength are evaluated for the specimens.

To accompany the experimental testing, a series of numerical simulations were conducted using commercial finite-element software to study the effects of randomly distributed heterogeneities on wave distortion in a controlled environment. In these simulations, randomly generated heterogeneities are scattered throughout a 2D plate with materials properties different from the bulk material. Ultrasonic wave propagation is simulated within this heterogeneous medium to investigate the effects of the heterogeneities' elastic properties, geometry, and distribution on ultrasonic signals, including distortion measured in terms of higher harmonic generation (HHG).

Experimental results indicate correlations between the nonlinearity parameter and both ultimate tensile strength and yield strength, where nonlinearity generally decreases as these mechanical parameters increase, particularly in the AM samples. We hypothesize that microstructural changes in grain size and distribution through the heat treatment process influence these trends in measured nonlinearity. Additionally, substructures at even smaller length scales, such as nanoscale precipitates and dislocations affect the ultrasonic and mechanical behavior. Measurements of elastic moduli and total elongation do not exhibit trends with the nonlinearity parameter. The linear parameter, wave speed, does not correlate well with the mechanical parameters, which is attributed to its lack of sensitivity to detect changes in microscopic features. These results show promising evidence for the feasibility of AM parts qualification using nondestructive nonlinear ultrasonic testing.

Results of the simulations indicate that changes in heterogeneity size, volume fraction, and material property deviations from the bulk material affect HHG to varying degrees. As expected, heterogeneities of smaller sizes and volume fractions have a less significant effect.

However, at increasingly large values, changes in HHG are more pronounced, and material density and stiffness deviations from the bulk material are shown to have a larger effect on HHG.

Future work includes continuing nonlinear ultrasonic testing, as well as comparing results to nonlinear resonant ultrasound spectroscopy (NRUS). New geometries and materials will be tested to expand the dataset. Microstructures will be imaged using scanning and transmission electron microscopy (SEM, TEM) and evaluate our hypotheses, and further complexity in numerical simulations will be implemented to isolate microstructural features and explore their effects on material behavior.

## NONTECHNICAL ABSTRACT

Additive manufacturing, also known as 3D printing, is a manufacturing method that differs from typical techniques such as machining. Rather than cutting away or subtracting from a solid block of material to create the final product, additive manufacturing builds the object one layer at a time. Industries such as defense, aviation, and transportation have the potential to benefit from the wider use of metal additive manufacturing techniques because they can improve efficiency, reduce waste, and allow for more agile production.

The major issue that prohibits the wider use of additively manufactured (AM) parts in these industries is the quality assurance of the AM components. During the layer-by-layer build of an AM part, very small flaws and defects can be introduced into the material that do not occur during traditional processes. For example, a small hole or missing material, called a pore, often appears in layers. These defects weaken the parts and could cause unexpected failure during their service life. For safety-critical applications, such as in airplanes or cars, this is unacceptable. To ensure that additive manufacturing is safe for use in these settings, a fast, accurate, and reliable method to detect these flaws must be established.

We propose the use of ultrasonic testing to detect the flaws within an AM material. High-frequency ultrasonic waves traveling through the part have sensitivities to these defects. We measure the ultrasonic behavior and strength properties of AM and traditional steel with the intent to understand their relationships. We also use computer models to simulate these tests, so we can control the types of defects and estimate their effects on the material. Experimental results indicate relationships between measured ultrasonic parameters and strength properties, indicating the feasibility to use ultrasound for the evaluation of AM parts.

## TABLE OF CONTENTS

LIST OF FIGURES .....	ix
LIST OF TABLES .....	xii
ACKNOWLEDGEMENTS .....	xiii
Chapter 1 Introduction .....	1
Chapter 2 Background .....	4
Linear Ultrasonic Techniques .....	4
Nonlinear Ultrasonic Techniques .....	6
Review of the Equations Governing Nonlinear Wave Propagation .....	6
Second Harmonic Generation .....	9
Nonlinear Resonance Ultrasound Spectroscopy (NRUS) .....	12
Analytical and Numerical Modeling of Wave Propagation .....	14
Nonlinear Ultrasonic Testing of Additively Manufactured Metals .....	17
Chapter 3 Numerical Modeling .....	20
Model Creation .....	20
Modeling the Effects of Heterogeneities on Elastic Wave Propagation .....	24
Chapter 4 Experimental Design and Data Analysis .....	29
Constituent Material and Sample Preparation .....	29
Mechanical Testing .....	31
Discussion of Ultrasonic Testing Protocols .....	32
Second Harmonic Generation Testing Protocol .....	32
Pulse-Echo Testing Protocol .....	35
Data Analysis .....	37
SHG Data Analysis .....	37
Pulse-Echo Data Analysis .....	41
Chapter 5 Results of Numerical Modeling .....	43
The Effect of Incident Amplitude on Higher Harmonic Generation .....	44
The Effects of Particle Size on Higher Harmonic Generation .....	46
The Effects of Particle Volume Fraction on Higher Harmonic Generation .....	47
Chapter 6 Experimental Results .....	50
Results of Mechanical Testing .....	50
Results of Ultrasonic Testing .....	53

Relationships Between Ultrasonic and Mechanical Parameters..... 56

Chapter 7 Discussion ..... 62

Chapter 8 Conclusion and Future Work ..... 68

Appendix A MATLAB Script for Ultrasonic Data Analysis..... 71

Appendix B Python Script for ABAQUS Simulations ..... 79

References..... 87

## LIST OF FIGURES

- Figure **2-1**: A schematic depicting the differences between nonlinear surface and bulk wave ultrasonic testing. The drawing shows example transducer orientations, as well as the interrogated region for each wave mode. .... 10
- Figure **3-1**: A schematic of the plate model showing boundary conditions, loading, and area of the received waveform..... 22
- Figure **3-2**: **(a)** Time domain response of the base model; **(b)** Frequency domain of the received signal. .... 24
- Figure **3-3**: Three examples of randomly generated heterogeneities in the 10x10 mm<sup>2</sup> bulk medium. These particles have a radius of 50 μm and represent a 5% volume of particles..... 25
- Figure **3-4**: A comparison of the “fully homogeneous” received signal plotted alongside the “matching properties” model where the distributed particles had identical properties to the bulk material. .... 26
- Figure **3-5**: An enlarged area of the heterogeneous microstructure after meshing. The heterogeneities have a radius of 50 μm. .... 26
- Figure **3-6**: The relationship between porosity and wave velocity in a simulated CrCo plate. These results are in agreement with the experimental reporting of [34]. ... 27
- Figure **4-1**: The resulting stress-strain curves from uniaxial tensile tests of **(a)** both AM and wrought (W) samples. **(b)** Includes just the wrought samples, and **(c)** the AM samples. Note the effect of the extensometer reset in each curve, exemplified by the small vertical line near the midpoint of each test. .... 32
- Figure **4-2**: A schematic of nonlinear bulk wave SHG testing. .... 33
- Figure **4-3**: The transducer fixture utilized for SHG testing. The 5 MHz transducer (left) emits an ultrasonic pulse with a frequency of 5 MHz. After propagating through the 10 mm thickness of the sample, the signal is received by a 10 MHz transducer (right). .... 34
- Figure **4-4**: A schematic of the linear pulse-echo testing equipment..... 36
- Figure **4-5**: Example of transducer orientation for pulse-echo testing on top of a foam block. .... 37
- Figure **4-6**: Examples of the data analysis steps for SHG testing. These measurements are from plate W-1100-3. The Hann window plotted with the original signal is shown in **(a)**. The frequency spectrum of the windowed signal is shown in **(b)**. Peaks A<sub>1</sub> and

$A_2$  are marked. The evolution of  $A_2$  vs.  $A_1^2$  for the 20 increasing amplitudes is shown in (c). The repeatability results of seven independent tests at the same location are shown in (d)..... 39

Figure 4-7: A representation of the change in the exponential relationship  $n$  between  $A_2$  and  $A_1$ . (a) Shows the result for the entire range of 20 amplitudes, while (b) demonstrates the change in slope from the removal of the highest amplitude data points. This data shown corresponds to sample W-1100-3. .... 41

Figure 4-8: An example of a received pulse-echo signal..... 42

Figure 5-1: Amplitude study on a plate with distributed heterogeneities with properties matching the bulk material. Observe no HHG at 10 MHz. .... 44

Figure 5-2:  $A_2$  vs.  $A_1^2$  where incident amplitude varies from  $1E-7$  to  $5E-6$ . (a) The FFT for each increasing amplitude. (b) The ratio of second harmonic peak  $A_2$  to fundamental  $A_1^2$ ..... 45

Figure 5-3: The influence of particle radius on wave distortion for material properties of Study 1 and Study 2. (a) Changes in wave distortion ( $A_2/A_1^2$ ), and (b) wave velocity.46

Figure 5-4: The influence of volume fraction of heterogeneities on wave distortion for material properties of Study 1 and Study 2. (a) Changes in HHG ( $A_2/A_1^2$ ), and (b) wave velocity. .... 48

Figure 6-1: The results of mechanical testing on both wrought and AM components: (a) Ultimate Tensile Strength, and (b) Yield Strength..... 51

Figure 6-2: The results of mechanical testing on both wrought and AM components: (a) Elastic Moduli, and (b) Total Elongation..... 52

Figure 6-3: The results of nonlinear SHG testing on both wrought and AM components: (a) Detailed individual plate results, and (b) overall results for each heat treatment. 54

Figure 6-4: The results of linear pulse-echo testing on both wrought and AM components: (a) Detailed plate results, and (b) overall results for each heat treatment. .... 55

Figure 6-5: Combined results of YS and ultrasonic testing: (a) YS plotted against the nonlinearity parameter  $\beta'$  in AM samples, and (b) linear wave speed in AM samples. (c) and (d) show the results of  $\beta'$  and wave speed for wrought samples..... 57

Figure 6-6: Combined results of UTS and ultrasonic testing: (a) UTS plotted against the nonlinearity parameter  $\beta'$  in AM samples, and (b) linear wave speed in AM samples. (c) and (d) show the results of  $\beta'$  and wave speed for wrought samples..... 58

Figure 6-7: Combined results of Elastic Moduli and ultrasonic testing: **(a)** Elastic Moduli plotted against the nonlinearity parameter  $\beta'$  in AM samples, and **(b)** linear wave speed in AM samples. **(c)** and **(d)** show the results of  $\beta'$  and wave speed for wrought samples. .... 59

Figure 6-8: Combined results of total elongation and ultrasonic testing: **(a)** Total elongation plotted against the nonlinearity parameter  $\beta'$  in AM samples, and **(b)** linear wave speed in AM samples. **(c)** and **(d)** show the results of  $\beta'$  and wave speed for wrought samples. .... 60

**LIST OF TABLES**

Table 3-1: Material properties of the homogeneous plate model. ....	21
Table 4-1: Chemical composition of 316L stainless steel (wt%) .....	30
Table 4-2: Name, heat treatment information, and number of each sample.....	30
Table 5-1: Material properties of the distributed heterogeneities in each study.....	43

## ACKNOWLEDGEMENTS

I would like to thank my advisors, Parisa Shokouhi and Matthew Lear, for their guidance and ongoing support during my studies and research, as well as Jeremy Schreiber for his knowledge and role in my committee. I would also like to thank Dr. Jacques Rivière, the Shokouhi/Rivière lab group, and all the members of PennSUL who have assisted me during this project, with special thanks to Michail Skiadopoulos for educating me in crucial aspects of my simulations. Finally, thank you to Carly Donahue and Colt Montgomery of the Los Alamos National Laboratory for the creation of the sample set used during testing, and their correspondence over the past year.

## Chapter 1

### Introduction

The significance of additive manufacturing across a diverse range of industries is growing. Recent advancements in manufacturing technology have offered the potential to disrupt traditional methods such as forging or casting components. In January 2021, the United States Department of Defense (DoD) published the first edition of its comprehensive additive manufacturing strategy outlining plans to integrate, expand, promote, and secure additive manufacturing as a modernized and agile technique for the future [1]. Sometimes referred to as “3D printing,” additive manufacturing provides a means of rapid prototyping and building custom-designed parts which increases flexibility, shortens the supply chain, and reduces materials waste.

A well-recognized barrier to the wider adoption of additive manufacturing in industry is the lack of effective approaches for qualification and certification, particularly for structural and safety-critical components. In their report, the DoD identified five primary barriers that must be overcome to capitalize on the additive manufacturing revolution, the first of which regards generating rapid, standardized approaches for qualification. Because AM parts are fabricated differently than typical forged or cast components, different sets of volumetric imperfections on a range of scales are present within the parts. Two examples of these imperfections are microscale gas porosities ( $\sim 10 \mu\text{m}$ ) and lack-of-fusion defects ( $\sim 100 \mu\text{m}$ ). Further, different processing parameters such as laser power or scanning speed can drastically alter the microstructural properties in AM parts of the same material.

Among existing nondestructive evaluation (NDE) methods for AM parts qualification, x-ray micro-computed tomography ( $\mu$ CT) is the standard for evaluating safety-critical components. For example, studies by Van Bael [2] and Pyka [3] demonstrate the capability of x-ray  $\mu$ CT in examining parameters of Ti-6Al-4V materials. Despite the ability of x-ray  $\mu$ CT to characterize AM samples, there are prohibitive factors associated with the technique. These include difficulty in transporting the equipment, the high cost associated with the scans, and limited resolution in large or complex geometries. These setbacks are significant in the wider adoption of an efficient, in situ testing solution.

Due to the challenges associated with scaling x-ray  $\mu$ CT to the additive manufacturing production levels identified by the DoD and other reviewers ([4],[5]), researchers have been assessing the capability of ultrasonic testing as an economic alternative for the assessment of performance-critical components with a range of geometric complexity. The objective of this research is to investigate the feasibility of linear and nonlinear ultrasonic testing parameters, which measure the distortion in elastic waves in the presence of microstructural heterogeneities, to represent the linkage between microscale features and the macroscale behaviors in AM parts.

To accomplish this objective, we will use a novel combination of numerical simulations and experimental testing. Our goal is to fundamentally understand the contributions of various microstructural heterogeneities present in a material (precipitates, voids, grain boundaries, dislocations, etc.) to its measured linear and nonlinear responses. A major challenge in studies of this nature is the cost associated with generating sufficiently large sample sets with well-understood microstructures and different geometries. By introducing numerical simulations into the process, synthetic data sets can be generated to complement those used during physical testing.

The organization of this thesis is as follows: a background section containing ultrasonic methods, simulations, and current state-of-the-art is provided in Chapter 2. Chapters 3 and 4 provide the numerical and experimental design, respectively. Chapter 5 shows the results of the numerical studies. Chapter 6 shows the results of the mechanical and ultrasonic testing. Finally, Chapter 7 contains a discussion of results, followed by concluding remarks and future work in Chapter 8.

## Chapter 2

### Background

The fundamental theories that define this research are multidisciplinary, spanning the fields of engineering mechanics, materials characterization, wave physics, and numerical modeling. The intersection of these different disciplines enables a complete study into not only the macroscale elastic behavior, but also the microscale properties which contribute to these responses. This literature review will begin with a brief discussion of linear ultrasound and its limitations, leading to the necessity for nonlinear methods. Concepts in nonlinear ultrasonic testing are discussed, followed by multiscale microstructural modeling using both numerical and analytical methods. The next section will discuss additive manufacturing in metals from the lens of the ultrasonic techniques used to characterize these materials.

### Linear Ultrasonic Techniques

Before the discussion of nonlinear ultrasonic methods that are critical to our hypothesis, a brief discussion of linear (conventional) ultrasonic testing is necessary. Fundamental features of linear ultrasonic tests are a high-frequency emitted signal (on the order of MHz) propagating through a homogeneous material with the assumption that the shape of the emitted wave is not altered or distorted during its travel. If wave distortion must be accounted for, nonlinear wave theory must be introduced.

Commonly extracted parameters from linear ultrasonic testing include wave speed and attenuation. Through the measurement of the longitudinal and shear wave velocities, material

characteristics such as Poisson's ratio and the elastic moduli can be estimated nondestructively. Another common application of linear ultrasonic testing is the characterization of volumetric flaws embedded within a material.

Attenuation represents the loss of energy that a wave experiences during its propagation due to factors such as scattering and absorption. Attenuation has been shown to demonstrate sensitivity to microstructural features of a material, such as the grain size and the distribution of second-phase particles [6]. Linear parameters are frequently presented alongside more sensitive nonlinear ultrasonic parameters to provide additional insights into the sample's behavior. In the research presented in this thesis, wave speed is reported.

Linear ultrasonic techniques offer effective solutions in industry for tasks including the volumetric detection of corrosion defects [7] and inspection of weld quality [8]. However, the constraint of linear ultrasonic measurements is its limited resolution – only features on the same order of magnitude as the incident wavelength can be detected. For microscopic features that are orders of magnitude smaller than the incident wave ( $\mu\text{m}$ ,  $\text{nm}$ ), linear techniques are not effective [9]. Sensitivity issues in linear ultrasound have been reported as early as the 1980s, when Sinclair and Eng were unsuccessful in utilizing linear ultrasonic measurements for the characterization of fracture toughness in steel samples [10]. Due to the microscale heterogeneities that contribute to changes in fracture toughness, velocity and attenuation were not sensitive enough to capture its behavior.

The goal of quality assurance in AM components requires the need to evaluate microscale features such as voids, precipitates, and dislocations. For this reason, nonlinear ultrasonic techniques with significantly higher resolution are chosen over conventional methods.

In the next section, background information will be discussed on nonlinear ultrasonic measurements, followed by examples of their utility in literature.

### **Nonlinear Ultrasonic Techniques**

Where linear ultrasonic methods are only capable of characterizing features on the same order of magnitude as the incident wave, nonlinear ultrasonic testing offers the ability to measure features on length scales that are orders of magnitude smaller. Although several nonlinear tests exist in the field of ultrasonic evaluation, two methods possess notable utility for the characterization of microstructural features within a material: Second Harmonic Generation (SHG) and Nonlinear Resonance Ultrasound Spectroscopy (NRUS).

### **Review of the Equations Governing Nonlinear Wave Propagation**

The following equations will be derived considering the one-dimensional longitudinal wave mode propagating in the x-direction of a nonlinear elastic medium with the following constitutive relationship:

$$\sigma_{xx} = \sigma_0 + E_1 \left( \frac{\partial u}{\partial x} \right) + \frac{1}{2} E_2 \left( \frac{\partial^2 u}{\partial x^2} \right) + \dots, \quad (1)$$

where  $\sigma_{xx}$  is the normal stress along the x-direction,  $u$  is the displacement, and  $E_1, E_2$  are second and third-order elastic constants. It should be noted that this nonlinearity is rooted in the physics

interaction within microstructure, not a large deformation or geometric nonlinearity. The equation of motion for this system is:

$$\frac{\partial \sigma_{xx}}{\partial x} = \rho_0 \frac{\partial^2 u}{\partial t^2}, \quad (2)$$

where  $\rho_0$  is the material density, and  $t$  is time. With these equations, the nonlinear wave equation can be expressed as:

$$\frac{d^2 u}{dt^2} = c^2 \left(1 - \beta \frac{\partial u}{\partial x}\right) \frac{d^2 u}{dx^2}, \quad (3)$$

where  $c$  is the longitudinal wave speed, and  $\beta$  is the nonlinearity parameter. In further detail,  $\beta$  can be expressed as a function of second and third-order elastic constants:

$$\beta = -\left(\frac{3C_{11} + C_{111}}{\sigma_0 + C_{11}}\right) = -\left(\frac{3}{2} + \frac{C_{111}}{2\rho_0 c_l^2}\right), \quad (4)$$

where  $C_{11}$  and  $C_{111}$  represent second and third-order Brugger elastic constants. Assuming plane wave propagation and the nonlinearity is small, Equation 3 can be separated and solved using the method of perturbation and expressed as:

$$u = U_1 \sin(kx - \omega t) + \frac{\beta U_1^2 k^2 x}{8} \cos(2kx - 2\omega t), \quad (5)$$

where  $U_1$  represents the amplitude of the fundamental harmonic wave propagating with speed  $c$ , radial frequency  $\omega$ , and wavenumber  $k = \frac{\omega}{c}$ . It is useful to denote  $\frac{\beta U_1^2 k^2 x}{8}$  as  $U_2$ , or the amplitude of the second harmonic.  $U_2$  can be rearranged to solve for  $\beta$  as a function of the harmonic amplitudes:

$$\beta = \frac{8U_2}{U_1^2 k^2 x}. \quad (6)$$

To measure the relative nonlinearity parameter, experiments are carefully constructed so that the environment and protocol are held constant. Examples include using transducers of the same frequencies for every measurement, and manufacturing specimens of the same thickness. Details of the experimental protocols are found in Chapter 4.  $U_1$  and  $U_2$  are commonly denoted as  $A_1$  and  $A_2$ , representing the attenuated amplitudes from SHG testing. The following equation is used for the estimation of the relative nonlinearity parameter:

$$\beta' = \frac{A_2}{A_1^2}. \quad (7)$$

With this relationship, the relative nonlinearity parameter can be expressed as the relationship between the fundamental and second harmonic amplitudes measured during SHG testing. Other influential factors that affect  $\beta$  include source nonlinearities, propagation distance (particularly for surface waves), diffraction, and attenuation. Although setting correction factors and calibrating these parameters is crucial for the measurement of absolute  $\beta$ , they do not have a significant impact on the relative trends that are reported in these experiments.

## Second Harmonic Generation

The technique of SHG is a subset of HHG, or the measurement of the peak amplitudes of higher harmonics in the frequency spectrum of the received waveform. As a uniform sinusoidal wave of frequency  $f$  propagates through a medium and interacts with its microstructural features, the waveform becomes distorted. This distortion grows cumulatively with propagation distance and is quantified through the measurement of the higher harmonic peaks ( $2f$ ,  $3f$ , etc.) which are visible in the frequency spectrum of the received signal. Normalizing the higher harmonic peaks against the fundamental amplitude provides an estimation for the classical nonlinearity parameters  $\beta$ ,  $\gamma$ , etc. Chapter 3 provides additional detail into the equations which govern SHG theory.

SHG has been shown to be sensitive in detecting microstructural changes in metals from several different sources. The evolution of microcracks, crystalline structure, and localized strain due to features such as dislocations, precipitates, and grain boundaries all have been *qualitatively* attributed to influencing the nonlinear ultrasonic parameters [11]. However, due to the complex interactions between these microstructural features at different length scales, *quantitative* or analytical relationships between micro-mechanical mechanisms and ultrasonic testing parameters do not yet exist.

Despite this, SHG testing has numerous applications in both research and in situ analysis. Different wave modes are compatible with SHG testing, including longitudinal (bulk) waves and Rayleigh (surface) waves. Lamb (plate) waves have also been studied for their use in SHG testing, however, they are less common as their dispersive behavior increases the complexity of these experiments [12]. The differences between bulk and surface wave SHG are schematically illustrated in Figure 2-1.

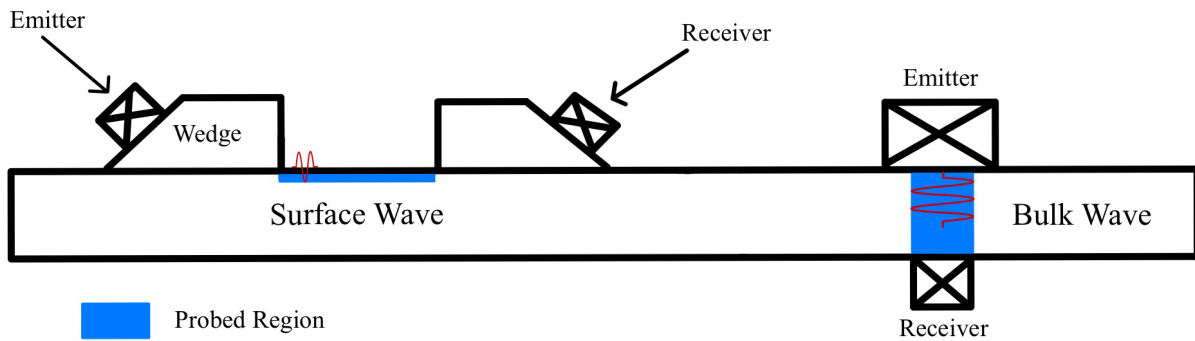


Figure 2-1: A schematic depicting the differences between nonlinear surface and bulk wave ultrasonic testing. The drawing shows example transducer orientations, as well as the interrogated region for each wave mode.

In bulk and surface wave SHG applications, the majority of literature reports relative measurements of the nonlinearity parameters, often denoted as  $\beta'$ . Measuring the relative nonlinearity parameter using piezoelectric contact transducers in bulk or surface wave modes allows for the construction of experiments using common ultrasonic laboratory equipment.

Measurement of the absolute nonlinearity parameter is also achievable and is desirable for its potential to enable quantitative evaluation. Park et al. recently measured absolute  $\beta$  in both copper and 6061 aluminum using a non-contact laser-ultrasonic method [13]. The results were validated with results from prior studies of absolute  $\beta$ , including those of Yost, Cantrell, and Breazeale [14]. Although the efforts to measure absolute  $\beta$  have been successful, they demand complex equipment, sensitive calibration, and are easily affected by surface roughness and damage. These challenges do not yet enable the adoption of absolute measurements for wider NDE applications [13].

SHG has been used extensively as a nondestructive method for characterizing the evolution of damage within a material, for example, under the presence of propagating microcracks in a fatigue test or the effects of heat-treatment on microstructure. In one study, the

onset of microcracking in steel-reinforced concrete coincided with a tenfold increase in  $\beta'$ , suggesting its application in engineering surveys of concrete structures [15]. Ultrasonic measurements in these settings demonstrate the potential to increase the efficiency of structural health monitoring when compared to visual and microscopic inspections.

Zhang et al. used Rayleigh waves to measure velocity, attenuation, and  $\beta'$  in aluminum 6061 samples which were artificially aged through a series of heat treatments [16]. Their results indicate a correlation between nonlinearity parameters and sample hardness which is attributed to the precipitates within the aluminum. Also, they suggest Rayleigh wave attenuation is an effective linear technique for monitoring microstructural changes. Nonlinear Rayleigh wave testing also demonstrated sensitivity to different levels of near-surface residual stress in shot-peened AA 7075, suggesting the potential for its use during in situ residual stress measurements at the near-surface [17].

SHG testing has been studied for the estimation of fracture toughness in steel samples. Jeong et al. used a two-step process involving the nonlinear bulk wave SHG method on a series of heat-treated CrMoV steel samples, using fracture appearance transition temperature (FATT) as the link between  $\beta'$  and fracture toughness. First, FATT values were correlated to  $\beta'$ . Then, FATT values are used to estimate fracture toughness through literature, so that fracture toughness and  $\beta'$  could be correlated [18]. More recently, Williams et al. investigated the use of bulk and surface wave SHG for the estimation of fracture toughness in heat-treated 4130 steel plates [19]. Mechanical data from Charpy V-Notch (CVN) and hardness testing were correlated to linear and nonlinearity ultrasonic parameters of wave speed and  $\beta'$ . Findings indicated a monotonic trend between  $\beta'$  and CVN in bulk wave testing and surface wave testing, although

these trends are not the same. Both studies suggest the feasibility of a nondestructive method for the evaluation of fracture toughness.

Limitations and challenges associated with SHG testing are important considerations for experimental design. Due to the contact between transducers, couplant, and the sample surface, it is important to remove surface roughness and debris (rust, dirt, etc.) from the sample before testing. These factors can influence the nonlinear response significantly. Due to the sensitivity of the higher-order harmonic measurements, ensuring repeatability during data collection is prevalent. Also, the interrogated region of the material in SHG is only as large as the volume of the incident wave. For large heterogeneous geometries, multiple SHG at different locations across the sample may be necessary to capture its overall nonlinear behavior.

SHG is an accessible, sensitive, and nondestructive method for the detection of changes in microscopic features within a variety of materials. The relative and absolute measurements of  $\beta$  through SHG have demonstrated sensitivity to changes in microstructure from different sources, and its study for applications in NDE continues to grow. Recently, nonlinear ultrasonic testing for the characterization of AM materials has been a topic of research interest. The current state-of-the-art for ultrasonic testing of AM components is detailed in the last section of this chapter.

### **Nonlinear Resonance Ultrasound Spectroscopy (NRUS)**

NRUS differs from SHG in that it is a resonance-based testing method. The parameters which can be measured during NRUS include the hysteretic nonlinearity ( $\alpha$ ) and resonance frequency, a

linear parameter. Because NRUS is a resonance-based method, it is applicable to more complex geometries than SHG, as it interrogates the entirety of the sample at once.

To begin the NRUS process, the resonant frequency of the sample must first be identified. Next, the selected resonance frequencies continue to be monitored under increasing amplitudes of excitation. For a sample with microstructural defects or heterogeneities, a decrease in resonant frequency is anticipated when increasing the amplitude of excitation. The shift in resonant frequency normalized by the maximum strain results in estimations for  $\alpha$ . An additional advantage of NRUS is its testing setup. Minimal, even non-contact test setups between transducer and sample are achievable, making surface roughness a minimal consideration compared to SHG testing.

Maier et al. researched the effectiveness of non-contact NRUS measurements on precipitate-hardened stainless steel bars with different degrees of thermal aging. The air-coupled NRUS system allows for non-contact excitation and reception, removing the necessity to glue transducers onto the parts which may alter the nonlinear behavior. Results show that the linear resonance frequency monotonically increases with thermal aging time. Nonlinear measurements also increased with aging time, however, the trend is nonlinear, with the magnitude of the increase declining with thermal aging steps. The hysteretic nonlinearity parameter measured using NRUS was further shown to agree with the acoustic nonlinearity parameter measured through SHG of the same samples [20].

NRUS has even been proposed for the measurement of the acoustic nonlinearity parameter through an inversion technique in thin plates [21]. Theory was first presented to enable an estimation of  $\beta$  from NRUS parameters. The linear resonance frequency was inverted to estimate the second-order elastic constant ( $C_{11}$ ), while the shift in resonant frequency was

inverted to obtain the third-order elastic constant ( $C_{111}$ ). These two constants were then used to estimate  $\beta$ , with results showing good agreement with traditionally measured  $\beta$  in literature for materials including aluminum and copper. This work provides a linkage between different ultrasonic nonlinear techniques, whose combined use could be a potential aid in the quality control of AM components.

### **Analytical and Numerical Modeling of Wave Propagation**

Numerical simulation is motivated by an outstanding challenge in the effort to move towards quantitative models linking ultrasonic nonlinearity and materials behavior is the prohibitive cost associated with generating data sets of heterogeneities and manufacturing samples for testing. Not only is the cost of resources significant for AM techniques, but the mechanical testing and various material characterization processes (such as electron microscopy) involve extensive preparation (polishing, mounting, etc.) and execution. By leveraging numerical and analytical modeling, synthetic data sets can be created to accompany physical experimental data and help to overcome these challenges.

Two recent studies from Kamali et al. exemplify this research effort. The studies investigate the influence of microscale and mesoscale heterogeneities on HHG for metals undergoing uniform plastic deformation [22], [23]. In the experimental portion [22], aluminum 1100 samples were machined into dog-bone geometries, and uniform plastic deformation between 0.5 and 4.0% was applied incrementally. For each sample, bulk wave SHG was conducted for the measurement of  $\beta'$  and  $\gamma'$  (the third harmonic) at both the geometrically uniform gauge and nonuniform shoulder sections of the dog-bones. The results of the

experimental tests show both  $\beta'$  and  $\gamma'$  increase with plastic deformation at both test locations, with  $\gamma'$  increasing 2.8 times more than  $\beta'$  in the shoulder, and 3.8 times more in the uniform gauge section. This indicates the sensitivity of both parameters to plastic deformation, and increased sensitivity with  $\gamma'$ . Using finite element modeling, numerical simulations were created to emulate the experimental processes of loading, unloading, and ultrasonic testing [23]. Microscale heterogeneities were modeled using an elastic-plasticity model with isotropic hardening. Mesoscale heterogeneities were also explicitly modeled through the creation of elements with different material properties than the bulk material on the same order of magnitude as the incident wavelength ( $\sim 10 \mu\text{m}$ ). Results of numerical SHG show smaller increases in  $\beta'$  and  $\gamma'$  at the gauge (2% and 8%), while the shoulder area shows considerably greater increases (396% and 1130%). The results of the experimental and numerical studies indicate the sensitivity of nonlinear parameters to plastic deformation, with the third harmonic  $\gamma'$  demonstrating more sensitivity than  $\beta'$ . Additional simulations also indicate that among different heterogeneity characteristics, differences in the elastic moduli from the bulk material, referred to as “strength deviation” in this research, have the largest effect on HHG.

Van Pamel et al. published multiple studies in which 2D and 3D models are created with randomly generated grain distributions. A mesh convergence study was conducted which measured the amount of backscattering noise (dB) in the signal from a pulse-echo style test. After validating the models, attenuation and phase velocity measurements are simulated using through-transmission, and compared to established theoretical results for a range of grain sizes and incident frequencies. For both 2D and 3D models, the simulations show agreement with theory across a range of scattering regimes. These results suggest that although the model

constructions were simpler than physical microstructures, they are capable of accurately capturing the underlying physical phenomena [24], [25].

Analytical modeling of distributed defects was researched by Li et al. in a molybdenum matrix with copper particles. Citing the shortcomings of traditional microstructural models (such as the classic pinned-dislocation bowing model of Hikata et al. [26]) for their lack of ability to consider the interactions and time dependence of heterogeneities, they present an analytical phase-field model with the capabilities to account for the evolution of microstructural interactions between distributed defects and elastic wave propagation. The results of this model indicate that  $\beta$  increases with elastic inhomogeneity, whether the precipitates are harder or softer than the matrix. Also,  $\beta$  was found to increase with lattice mismatch strain and depends on precipitate size for a given volume fraction (1%) [27].

Continuing the discussion of analytical modeling of the nonlinearity parameter, Fuchs et al. derived a reduced-order model of nonlinearity based on the formation of misfit dislocation on the grain boundaries of sensitized 304L and 316L stainless steels [28]. This model differs from prior models of pinned dislocations in that it theorizes that dislocations formed between  $M_{23}C_6$  carbides and the bulk material at grain boundaries are a primary contributor to increases in  $\beta$ . The growth of these precipitates was modeled using thermodynamic software, and the growth model was verified in physical samples using TEM. Results indicated that for both materials, the changes in  $\beta$  predicted by the model were similar to the experimental measurements. The findings suggest the utility of a combination of characterization, modeling, and experiments is viable for advancing the knowledge of nonlinear ultrasonic evaluation of features within steel.

A combination of analytic and numerical modeling combined with experimental characterization and testing is essential to advance the quantitative study of which

microstructural features affect nonlinearity, and to what extent. The studies cited here offer insight into the recent state-of-the-art results and discussion and provide examples of the fundamental ideas that drive the research presented through the experiments and simulations presented in the following chapters. The next section of this literature review discusses recent experimental work in the ultrasonic characterization of AM materials.

### **Nonlinear Ultrasonic Testing of Additively Manufactured Metals**

Recently, the feasibility of ultrasonic testing for the characterization, certification, and qualification of AM metals has been a focus of research efforts. Both SHG and NRUS methods have shown utility in the assessment of AM metals parts for parameters that are critical to the assessment of part quality.

Qiao and Yan studied the characterization of 316L stainless steel parts manufactured using selective laser melting (SLM). Microscopic defects such as pores and cracks introduced during the SLM process are attributed to their premature failure under fatigue loading. Using bulk-wave SHG, AM parts with different levels of internal fatigue damage were tested using ultrasound, followed by transmission electron microscopy and SEM. Results demonstrate a sensitivity of  $\beta'$  to the number of fatigue cycles in the material [29].

Bellotti et al. measured the ultrasonic response of AM materials using surface wave SHG testing. Both 316L and 304L stainless steel samples were tested, manufactured with wrought and additive manufacturing techniques. The additive manufacturing methods were L-PBF and laser engineering net shaping, both involving the deposition of a metal powder onto a substrate heated by a laser. Heat treatments are conducted on these samples to alter their microstructure, with

emphasis on studying dislocation density. Results indicate a distinction between the  $\beta'$  parameters measured in AM and wrought 316L samples. Quantitative analysis of dislocation density confirms the trend in ultrasonic results, that is, heat treatment reduces the density of dislocations in all manufacturing techniques and correlates with reduced values of  $\beta'$ . This trend does not maintain for the full range of heat treatments, as an increase in  $\beta'$  is measured between samples treated at 1050 and 1200 °C, attributed to different microstructural recrystallization at this temperature. Results further indicate a correlation between  $\beta'$  and hardness [30], [31].

NRUS has also been studied for the characterization of AM parts. A 2020 study from Kober et al. [32] used the nonlinear methods of Nonlinear Impact Modulation Spectroscopy (NIMS) on Ti-6Al-4V samples manufactured by selective electron beam melting to characterize porosity. Through the use of NIMS, an impact excitation (rather than an NRUS sweep) is applied, where the ring-down of this impact can be used to evaluate NRUS parameters. Due to the voids and lack-of-fusion defects present from the manufacturing process, the Ti-6Al-4V samples possess microstructures similar to granular media and exhibit hysteretic nonlinearity. Results showed that NRUS was able to distinguish the dense sample from those with porosity, however, the results did not correlate with porosity levels. This is encouraging for use in quality assurance, because it shows feasibility for NRUS to be used in a “pass/fail” method with respect to a normalized standard sample.

Bozek et al. studied cylindrical Ti-6Al-4V samples manufactured by L-PBF to investigate the utility of NRUS in the prediction of fatigue life [33]. The samples were tested both before and after hot isostatic pressing (HIPing), a thermal treatment to reduce the size of internal flaws and improve fatigue properties. The reduction of the volume of flaws from HIPing was verified by x-ray  $\mu$ CT. Results show before to HIPing, no NRUS parameters correlated with fatigue life,

however, both linear and nonlinear NRUS parameters show correlations with fatigue life post-HIPing. Samples with larger resonant frequencies showed increased fatigue life, and samples with higher nonlinearity exhibited shorter fatigue life due to the increased presence of flaws in their microstructure.

Although the use of ultrasonic testing to evaluate AM materials is a relatively new research area, the results of recent studies demonstrate the capabilities of both SHG and NRUS methods to characterize a variety of different material behaviors (dislocation density, porosity, fatigue life, etc.) through linear and nonlinear ultrasonic parameters. Future research will be critical to advance the understanding of the relationships between ultrasonic parameters, microstructure, and mechanical properties on an increasingly diverse set of materials, geometries, and microstructural features.

## Chapter 3

### Numerical Modeling

While the experimental measurements of nonlinearity using ultrasonic methods are excellent for identifying trends between various properties and nonlinear ultrasonic responses, a significant knowledge gap exists quantifying their microstructural origins. The fundamental set of simulations presented here aims to study the effects of varied microstructural heterogeneities within a material on HHG in a linear elastic medium. It should be noted that in this phase, we are not seeking to directly measure nonlinearity in these simulations, rather, the distortion of the elastic wave that leads to HHG. By limiting the model to be linear elastic in the beginning, future studies with more complex constitutive models will enable the ability to more clearly distinguish the origins of material behavior.

#### Model Creation

Before introducing heterogeneities into the model, a homogeneous model was generated to provide a baseline, undistorted result for comparison, as well as to test boundary conditions (BCs), mesh sizes, and implementation of the modeling script. Using Python scripting (Appendix B) together with ABAQUS, a commercial finite element software, a two-dimensional plate was modeled.

Creating a Python script to streamline model generation offers several benefits. Instead of reconstructing or altering the model repetitively in the graphical user interface (GUI) of ABAQUS, scripting increases efficiency in model creation. By assigning variables in the script such as the plate geometry, mesh size, and material properties, altering the model does not

require GUI intervention. Additionally, assigning certain BCs and randomly distributing heterogeneities through the model is significantly more efficient through scripting. The script can be designed so that multiple iterations of the simulation can be run in a loop without user interference. This is especially useful for parametric studies, where a single independent variable is modified in between each simulation to observe its effects. More details on these processes will be discussed later in this section.

The base model is a 10 x 10 mm<sup>2</sup> plate with steel material properties shown in Table 3-1. A homogeneous, linear elastic continuum is chosen to represent the plate. To facilitate the propagation of a longitudinal wave, a displacement BC is imposed on a node at the left edge of the model. Also, the bottom left corner of the plate is pinned in both the x and y-directions. The top right corner is pinned in the x-direction, while the bottom right corner is pinned in the y-direction.

Additionally, periodic boundary conditions (PBCs) are applied to the top and bottom edges of the model. PBCs facilitate the creation of an “infinite” model by repeating the behavior of the finite model. This enables the achievement of a longitudinal plane wave solution regardless of the direction of wave motion [25]. PBCs function by constraining the displacements, velocities, and accelerations of a node on one extremity of the model with its partner node at the same location on the opposite extremity.

Table 3-1: Material properties of the homogeneous plate model.

Density (kg/m <sup>3</sup> )	E (GPa)	G (GPa)	$\nu$
7,800	210.38	82.39	0.277

The loading used to simulate longitudinal wave propagation is applied as a displacement BC. Through the use of MATLAB, a tabular input signal is created. To represent the incident

waveform used in the experiential portion of this research, a 5 MHz, 10-cycle sinusoidal pulse with 250 MHz sampling frequency is used for the numerical model. This pulse is applied to a single node at the left-center edge, and the received signal is averaged from several nodes at the center of the right edge. Figure 3-1 shows a schematic of the plate with boundary conditions.

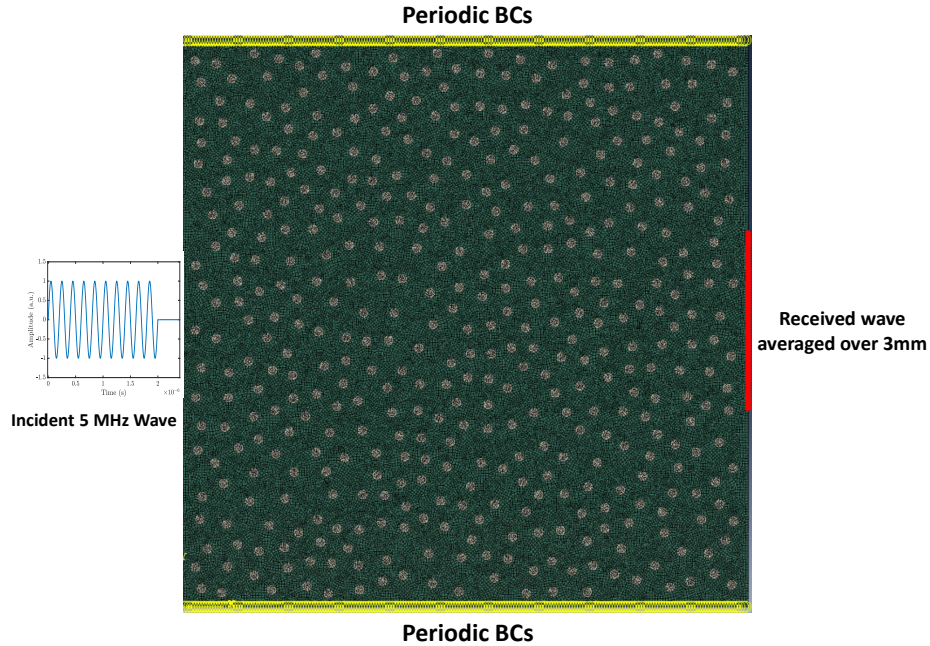


Figure 3-1: A schematic of the plate model showing boundary conditions, loading, and area of the received waveform.

The final consideration for the base model is meshing. To ensure both the accuracy and efficiency of the simulation, the mesh size should be chosen from the results of a convergence study. Details will be provided in the following section. In modeling dynamic wave propagation, it is common to choose a mesh size ( $h$ ) that is 10 to 20 times smaller than the wavelength ( $\lambda = \frac{c_l}{f}$ ) of the incident wave:

$$h \leq \frac{\lambda}{20}. \quad (8)$$

Similarly, the choice of time-step is governed by the Courant-Friedrichs-Lewy (CFL) relation for the convergence of solving partial differential equations:

$$\Delta t \leq \frac{1}{20f} . \quad (9)$$

In the base model, a mesh size of  $15/\lambda$  (or 0.078 mm) is chosen, while the time step is set to 4 ns. This time step is much smaller than the maximum allowed value from the CFL relation and intended to represent the 250 MHz sampling frequency chosen for the incident wave in experiments. Figure 3-2 shows the time domain and frequency domain responses of the homogeneous model. These results were generated from tabular output data of the received signal in ABAQUS post-processing, with the signal analysis done in MATLAB. As anticipated, the received signal is undistorted, and no higher harmonics are generated in the frequency spectrum.

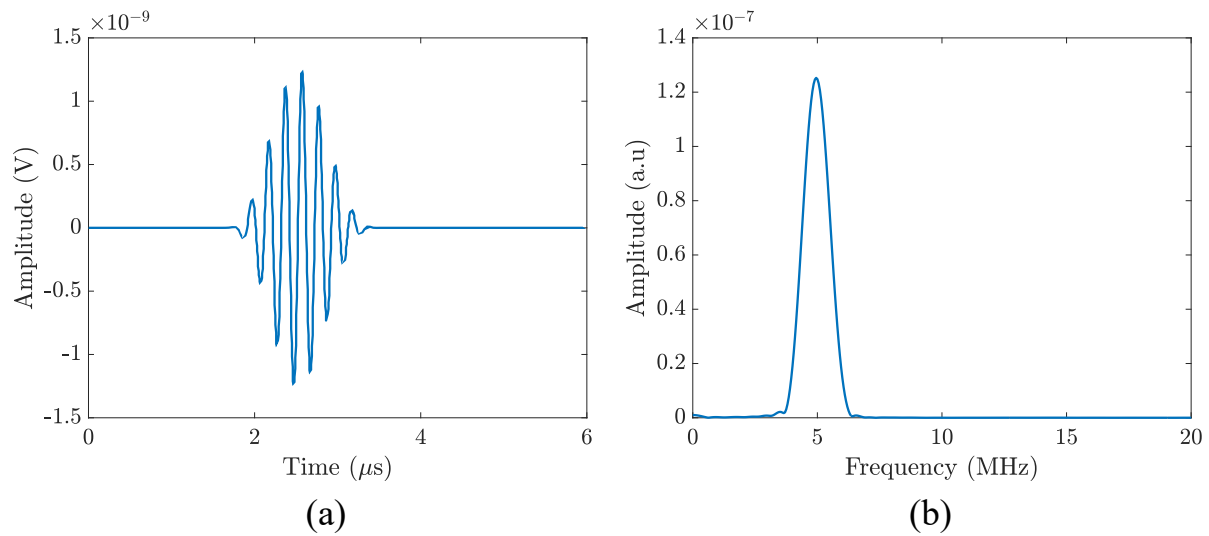


Figure 3-2: **(a)** Time domain response of the base model; **(b)** Frequency domain of the received signal.

### Modeling the Effects of Heterogeneities on Elastic Wave Propagation

With the homogeneous base model parameters established, randomly distributed heterogeneities can be introduced into the sample. Using the Python script, the parameters for creating the heterogeneities include size (radius), the minimum distance between heterogeneities, the volume fraction of heterogeneities, and the area to distribute them. Figure 3-3 shows three examples of randomly distributed heterogeneities created with the same input parameters. Additional functions are written to ensure two heterogeneities do not overlap or extend over the boundary of the plate. Options are available to control the material properties of the particles, so that they may differ from the bulk.

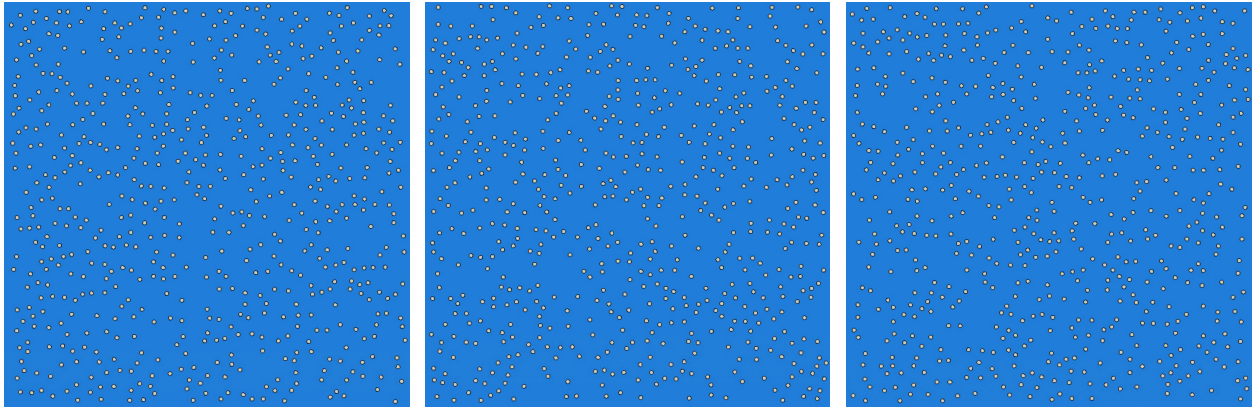


Figure 3-3: Three examples of randomly generated heterogeneities in the 10x10 mm<sup>2</sup> bulk medium. These particles have a radius of 50  $\mu\text{m}$  and represent a 5% volume of particles.

To validate the results of the model, two different experiments were conducted for comparison to baseline results. In the first study, heterogeneities were randomly distributed throughout the bulk material, however, their material properties were assigned to be *identical* to the bulk plate. In other words, a homogeneous microstructure was created that required the meshing complexity of the heterogeneous model. The radius of each heterogeneity was 50  $\mu\text{m}$ , with a 10% volume fraction. In both cases, no HHG or wave distortion resulted. A comparison of the received time domain signals between the “fully homogeneous” model and the “heterogeneous” model with matching properties yielded an error of less than 2%. Figure 3-4 shows these signals plotted simultaneously. The shape of each signal is nearly identical, there is a minor difference only in the amplitudes between them. The approximate element size was 0.03 mm, and 13 elements were meshed around the circumference of each heterogeneity. Figure 3-5 shows an enlarged example of the resulting mesh that is imposed on the heterogeneous microstructure with these parameters.

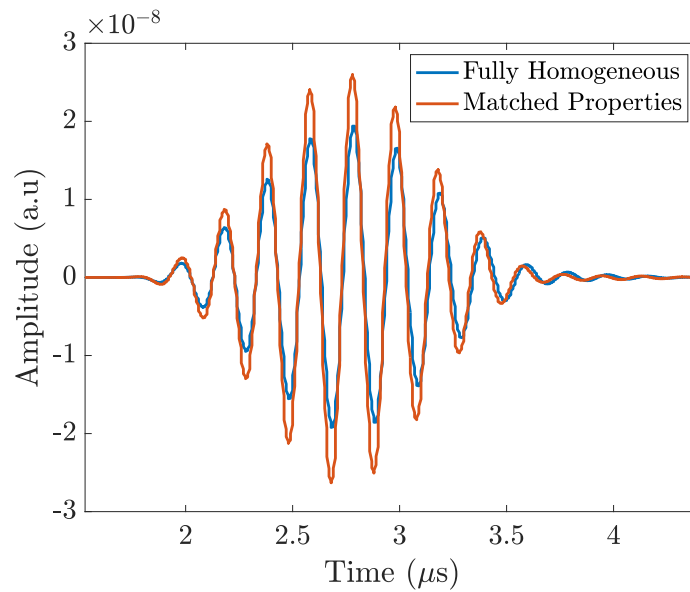


Figure 3-4: A comparison of the “fully homogeneous” received signal plotted alongside the “matching properties” model where the distributed particles had identical properties to the bulk material.

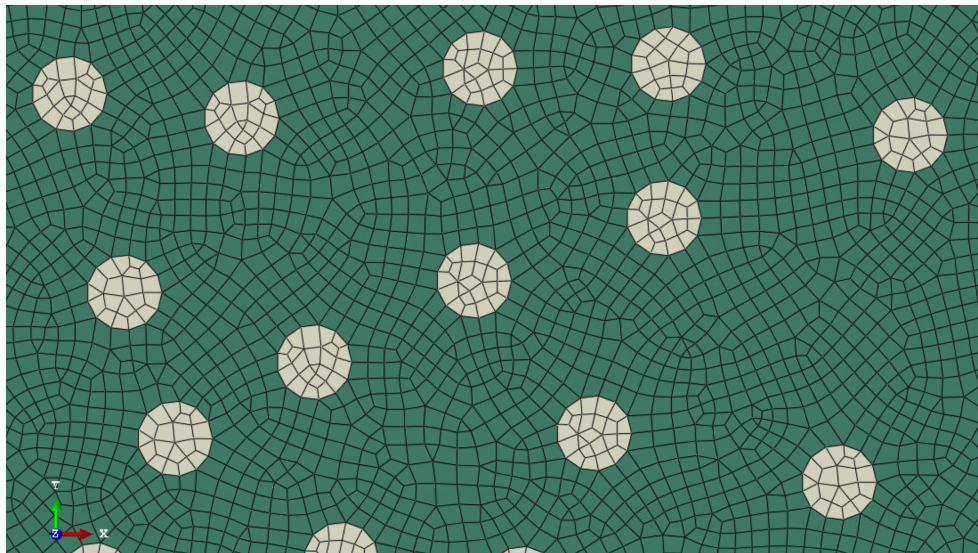


Figure 3-5: An enlarged area of the heterogeneous microstructure after meshing. The heterogeneities have a radius of  $50\ \mu\text{m}$ .

In the second validation study, heterogeneities were once again distributed within the model. However, rather than assigning them material properties, their material was subtracted from the plate, leaving behind a random distribution of voids. Porosity has well-documented

effects on wave propagation, notably a linearly decreasing relationship between wave speed and increasing volume fraction of pores [34].

To validate the effects of porosity on wave propagation in this model, an experimental study from Slotwinski et al. was simulated in CrCo alloy [34]. 50  $\mu\text{m}$  voids were distributed throughout the microstructure with volume fractions ranging from 1% to 10%, and the wave velocities of the received signals were recorded using an amplitude thresholding technique to estimate their arrival times. Figure 3-6 shows the results of this validation exercise for the simulations plotted alongside the analytical result. It can be observed that an increasing volume fraction of porosity has a linearly decreasing relationship with wave speed in accordance with the analytical findings in [34]. The error with respect to the analytical model is less than 4%.

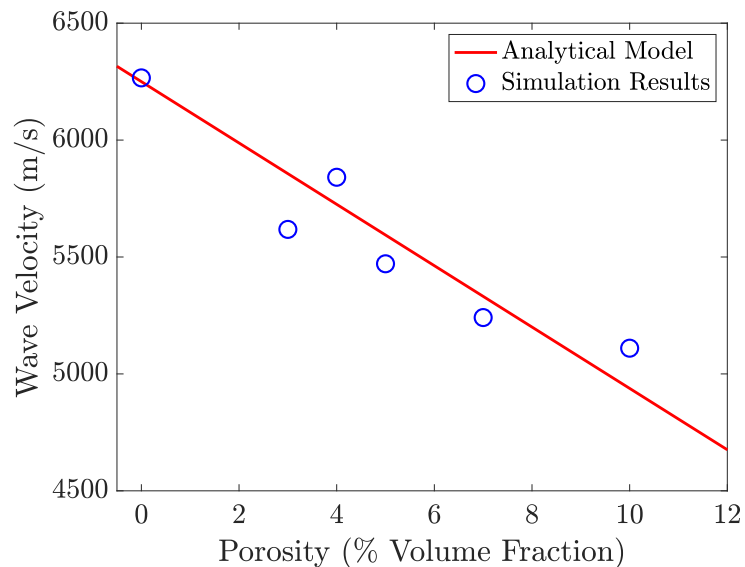


Figure 3-6: The relationship between porosity and wave velocity in a simulated CrCo plate. These results are in agreement with the experimental reporting of [34].

With the meshing and simulation validated, the next phase of experiments will investigate the effects of distributed heterogeneities with various changes in geometry and elastic

properties on HHG. Several different parametric studies are investigated for different heterogeneity properties, the results of which are shown in Chapter 5.

## Chapter 4

### Experimental Design and Data Analysis

Alongside the numerical studies, mechanical and ultrasonic tests were performed on a series of steel samples. This chapter will describe the experimental methods beginning with sample preparation. Then, the testing protocols for mechanical and ultrasonic testing are detailed, followed by the steps taken to analyze the ultrasonic data.

#### Constituent Material and Sample Preparation

The material used for this study is 316L stainless steel, a variation from 316 stainless steel characterized by its reduced carbon content. This offers increased corrosion resistance and better performance in high-temperature environments such as chemical manufacturing equipment and nuclear reactors [35]. Table 4-1 contains details about the chemical composition of 316L stainless steel, provided with ranges from different sources in literature [36], [37].

Two sets of specimens with different manufacturing techniques were created and heat-treated. The first set of samples was additively manufactured using an EOS M 290 L-PBF system. The laser power was set to 214.2 W, with a scan speed of 928.1 mm/s. The powder particles used for printing have a D90 distribution of 15-45  $\mu\text{m}$ . L-PBF functions through a laser source selectively binding or melting powder layer-by-layer to create a geometry. Although the samples in this study are simple rectangular plates, L-PBF can manufacture significantly more complex geometries. The second set of samples was cast using a standard wrought method. In

total, there are 21 AM samples and 20 wrought samples. The dimensions of these plates are 50 x 50 x 10 mm<sup>3</sup>.

Common process-related defects from L-PBF include high levels of residual stress, incomplete/lack of fusion defects, cracks from high cooling rates, and micro-roughness [38]. Large variations in mechanical properties of L-PBF components, such as ultimate tensile strength (UTS) and yield strength (YS) have been reported. For example, a review paper of L-PBF 316L parts in their as-built state listed UTS values between 512 – 703 MPa, depending on the print orientation and other parameters [38]. The sources of these variations are further discussed in Chapters 6 and 7.

Table 4-1: Chemical composition of 316L stainless steel (wt%)

C	Co	Cr	Cu	Mn	Mo	N	Ni	P
0.01-0.02	0.19	16.69-16.92	0.28	1.19-1.30	1.99-2.01	0.04	10.19-10.38	0.03-0.04

An annealing heat treatment process was conducted on the samples to induce microstructural changes to alter their mechanical and ultrasonic behavior. The heat treatments were conducted in a vacuum furnace for 1 hr at 10<sup>-5</sup> torr, followed by cooling in argon to prevent surface oxidation. For both the AM and wrought samples, four different heat treatment temperatures were used across the range of specimens: “as-built” (no heat treatment), 600 °C, 900 °C, and 1100 °C. Table 4-2 provides additional details on the samples.

Table 4-2: Name, heat treatment information, and number of each sample

Name	Wrought				AM			
	WAB	W-600	W-900	W-1100	AMAB	AM-600	AM-900	AM-1100
Heat Treatment	0 °C 0 hr	600 °C 1 hr	900 °C 1 hr	1100 °C 1 hr	0 °C 0 hr	600 °C 1 hr	900 °C 1 hr	1100 °C 1 hr
Number of Plates	5	5	5	5	6	5	5	5

## Mechanical Testing

For each manufacturing method and heat treatment, an additional set of samples were made for mechanical testing (uniaxial tensile test) conducted at Los Alamos National Laboratory. For each sample, three coupons were available for mechanical testing. The specimens were tested in a hydraulic tensile frame with pin-connector grips. A 12.7 mm extensometer was used to measure displacement at a strain rate of  $10^{-3} \text{ s}^{-1}$ . Stress and strain calculations were then calculated with respect to the starting gauge length of the extensometer and cross-sectional area of the samples.

To accommodate elongation exceeding 70% of the initial length and to continue the displacement measurements, the extensometer was reset during testing. The 12.7 mm extensometer used allows for a  $\pm 2.54$  mm displacement. To accommodate for the full displacement of the sample, the extensometer was depressed by -2 mm at the start of the testing, and allowed to extend to +2 mm, or a total travel of 4 mm. At this point, the testing was paused for approximately 30 s and the extensometer was depressed to -2 mm. Although visible on the stress-strain curve of the data, this reset is necessary to capture the mechanical behavior from initial conditions until failure.

From this testing, four mechanical parameters were extracted: UTS, YS, elastic moduli, and total elongation. Wrought and AM samples exhibited distinct mechanical responses. For the wrought samples, the elastic moduli were calculated from data between 100 and 200 MPa. In the AM components, this value ranged from 100 to 300 MPa. Data above 100 MPa was processed to ensure that nonlinear material behavior was not altering the elastic moduli calculations. The upper-stress limits were chosen such that the materials remained in the elastic regime associated with each manufacturing technique. Figure 4-1a shows the stress-strain curves generated for the

full set of samples, while Figures 4-1b and 4-1c show just the wrought and AM results, respectively. Detailed results of the mechanical testing experiments are shown in Section 6.

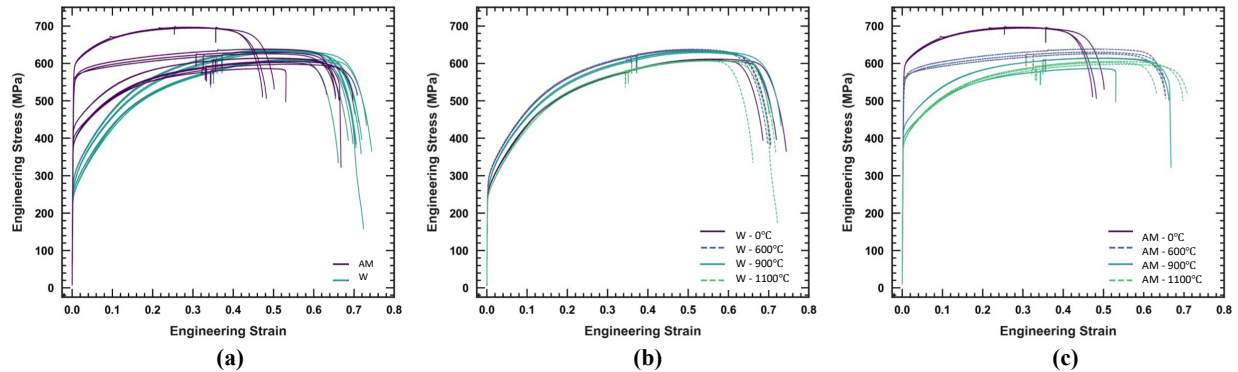


Figure 4-1: The resulting stress-strain curves from uniaxial tensile tests of (a) both AM and wrought (W) samples. (b) Includes just the wrought samples, and (c) the AM samples. Note the effect of the extensometer reset in each curve, exemplified by the small vertical line near the midpoint of each test.

### Discussion of Ultrasonic Testing Protocols

The ultrasonic testing procedure used during the bulk wave follows Williams et al. [19]. The parameters and equipment chosen for testing enable repeatable data collection and accurate measurements without sacrificing efficiency during the experimental procedures.

### Second Harmonic Generation Testing Protocol

Figure 4-2 depicts the data acquisition system used for bulk-wave SHG testing. To hold each transducer and improve the consistency of data acquisition, a custom-manufactured fixture (Leeman Geophysical LLC) was utilized as shown in Figure 4-3. This fixture provides additional

advantages for ensuring repeatability in each measurement, as the transducers are tightened by a threaded bolt with pressure provided by a spring located behind both the emitter and receiver.

This consistent pressure improves the contact between transducer element, coupling, and sample surface and improves upon the model used in [19].

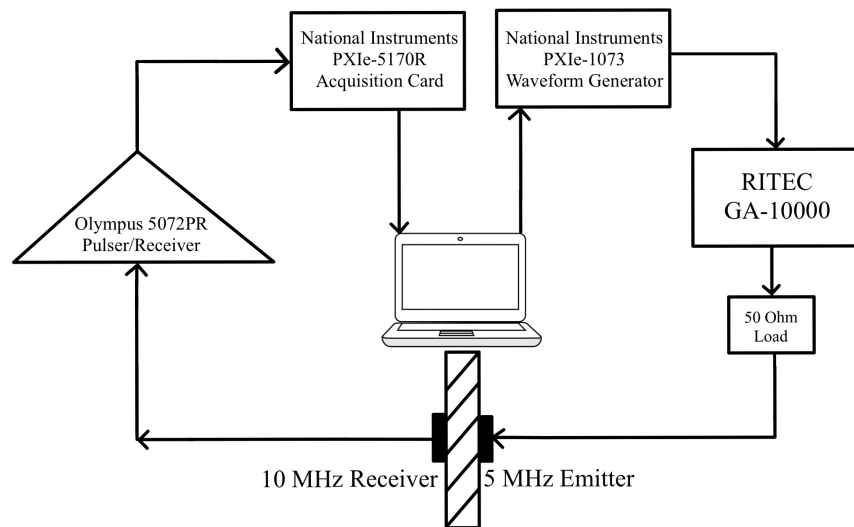
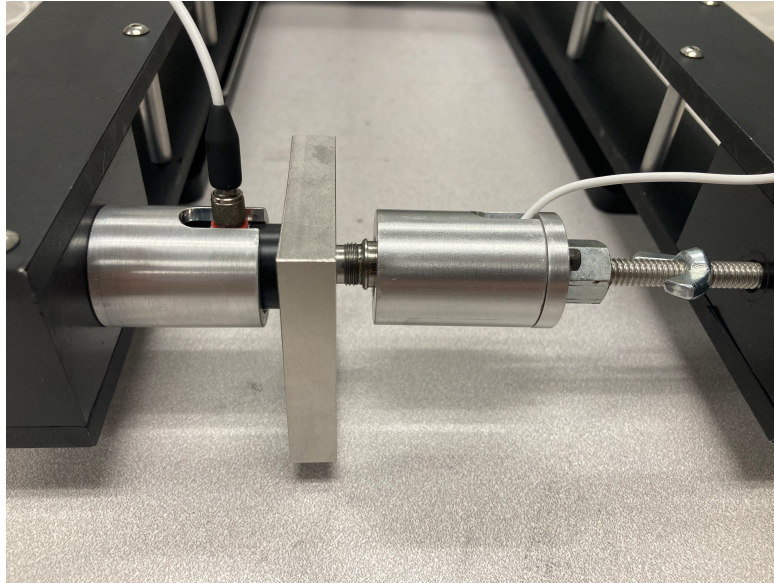


Figure 4-2: A schematic of nonlinear bulk wave SHG testing.

The equipment used for this setup includes an arbitrary waveform generation (PXIe-1073, National Instruments) connected to a Ritec higher-powered amplifier (GA-10000, Ritec) and 50  $\Omega$  load (RT-50, Ritec). A 5 MHz lithium niobate transducer (NdtXducer CML054) emits the ultrasonic signal, which propagates through the sample and is then received by a 10 MHz transducer (V544SM, Olympus). A preamplifier (5072PR, Olympus) with a gain of 15 dB is connected to the receiver, which connects to the National Instruments 5-slot chassis (PXIe-1073, National Instruments) with PXIe-5170R acquisition cards. The emitted wave is a 10-cycle tone burst pulse with center frequency of 5 MHz, and incident amplitudes ranging between 25 and 500 V in 25 V increments. The burst period is 10 ms, the sampling frequency is 250 MHz, and

the pulse repetition frequency is set to 100 Hz. To collect data, the chassis is connected to a Dell laptop equipped with a custom LabView program for the acquisition and real-time visualization of both the generated signal in the time and frequency domain.



**Figure 4-3:** The transducer fixture utilized for SHG testing. The 5 MHz transducer (left) emits an ultrasonic pulse with a frequency of 5 MHz. After propagating through the 10 mm thickness of the sample, the signal is received by a 10 MHz transducer (right).

For each plate, seven independent SHG tests are conducted at three arbitrarily chosen distinct locations, for a total of 21 tests per sample. This helps to ensure the results are representative of the entire sample and sufficient repeatability is achieved. To begin, ultrasonic gel (Magnaflux Soundsafe 20-012) is applied to both the emitter and receiver surfaces. To clean the sample, rubbing alcohol is applied to the surfaces with a cloth and dried. The sample is then inserted between the transducers, and the threaded bolt is tightened until both transducers are tight against the surfaces.

With the sample and transducers mounted, the SHG test begins. From a study of the time dependency of measurements (effects of couplant drying time on  $\beta'$ ) conducted in [19], testing

can confidently be completed immediately after mounting the sample. 20 ultrasonic pulses are emitted into the sample from 25 to 500 V, in increments of 25 V. The total time for these signals to be emitted is approximately 40 s. After each test, the transducers are uncoupled from the sample, and all surfaces are cleaned. New ultrasonic gel is then reapplied, and the process repeats. After seven complete tests are finished at one location, the transducers are moved to a new location on the plate for subsequent testing. The post-processing of this data will be discussed later in this chapter.

### **Pulse-Echo Testing Protocol**

To measure the wave speed of the samples, a different ultrasonic technique known as pulse-echo testing is utilized. In contrast to the through-transmission testing used during SHG, pulse-echo testing uses a single transducer as both the emitter and receiver and can provide a more accurate estimate of wave speed as the influence of coupling on pulse-echo measurements is negligible. The results of a pulse-echo test combined with a known sample geometry enable the calculation of linear ultrasonic parameters including wave speed and attenuation.

Figure 4-4 depicts the data acquisition system used during pulse-echo testing. Note that several components are the same in the SHG setup (Figure 4-2), including the pre-amplifier, arbitrary waveform generator, and acquisition cards. During pulse-echo testing, a lower voltage amplifier (TEGAM Model 2350) is used, because high voltages are not necessary to accurately measure the linear parameters. Additionally, a diplexer (RITEC) is required to facilitate the transmission and reception of the ultrasonic signal, combining multiple inputs from the amplifier

and transducer into a single output. This tool is necessary due to one transducer both emitting and receiving the ultrasonic signal.

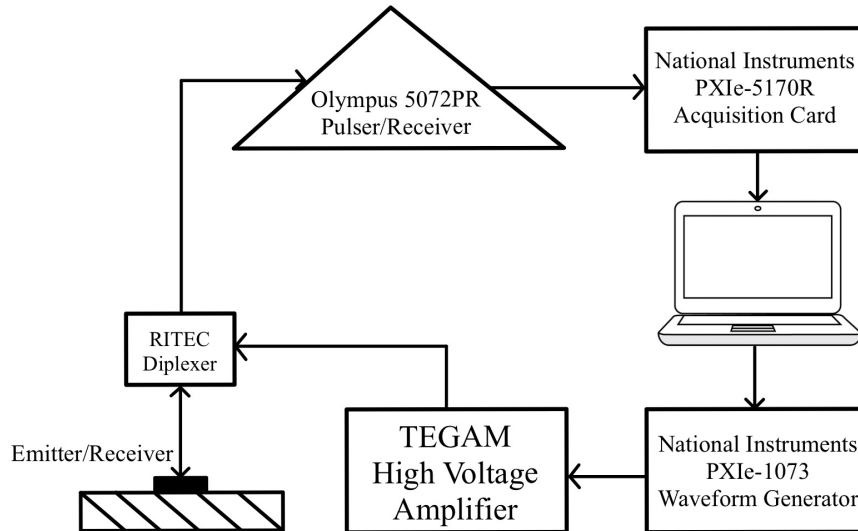


Figure 4-4: A schematic of the linear pulse-echo testing equipment.

A 2.5 MHz transducer (Olympus) is used for pulse-echo testing. The incident wave is a 4-cycle tone burst pulse with center frequency of 2.5 MHz. The amplitude of excitation is 50 V. The burst period is 10 ms, the sampling frequency is 250 MHz, and the pulse repetition frequency is set to 100 Hz. The gain on the pre-amplifier is set to 30 dB. The propagation of the longitudinal wave was recorded for 20  $\mu$ s to receive multiple reflections for analysis.

For each pulse-echo test, three total tests are conducted at independent locations on the sample. Note these locations are not the same as those used for SHG testing. The surface of the sample is cleaned according to protocol, and the same ultrasonic gel is applied to the transducer as in SHG testing. Light pressure is applied to the transducer during testing, and the tests are conducted on top of a foam block to eliminate influence from the laboratory table on the reflections as shown in Figure 4-5. A single pulse is emitted at each location, resulting in three

measurements per plate. In between testing, the sample and transducer are cleaned according to protocol. The analysis of pulse-echo data for the determination of wave speed will be described in the following section.



Figure 4-5: Example of transducer orientation for pulse-echo testing on top of a foam block.

### **Data Analysis**

To convert the recorded signal files into interpretable results for both SHG and pulse-echo testing, various signal processing techniques must be utilized. Using custom MATLAB scripts (available in Appendix A), the transition between raw data and measurable time domain and frequency domain results is achieved. Different methods are required for linear and nonlinear data, and both will be outlined in the following sections.

### **SHG Data Analysis**

To begin the data analysis process, the received time domain signal must be windowed to improve its quality in the frequency spectrum in the next steps. A Hanning (Hann) window is

selected, which gradually reduces both sides of the input signal to zero. The windowing effectively smooths the signal and minimizes its discontinuities. In the frequency spectrum, the Hann window reduces the side lobes and signal leakage, important to the accurate measurement of the peaks necessary for SHG testing. Figure **4-6a** demonstrates the difference between the original received signal and the Hann windowed signal in the time domain.

After windowing, the Fast Fourier Transform (FFT) of the windowed signal is computed and plotted as shown in Figure **4-6b**. This operation transforms the time signal for analysis of its frequency content. To more accurately calculate the amplitudes of the fundamental and second harmonic peaks, a parabola is fitted to the top five points of each peak, and the maximum amplitude of each parabola is chosen.

Figures **4-6a** and **4-6b** show the results of a single excitation amplitude. During SHG testing, we emit signals of 20 increasing amplitudes resulting in the 20 points plotted in Figure **4-6c**, where the x-axis denotes the magnitude of the fundamental harmonic peak squared at each amplitude, and the y-axis denotes the peak of the second harmonic at each amplitude. From the theory for measuring the relative nonlinearity parameter, the slope of this line is the estimation for  $\beta'$ . To ensure repeatability during the data collection process, seven independent trials for each plate location were measured. The repeatability of this data collection process is exhibited in Figure **4-6d**.

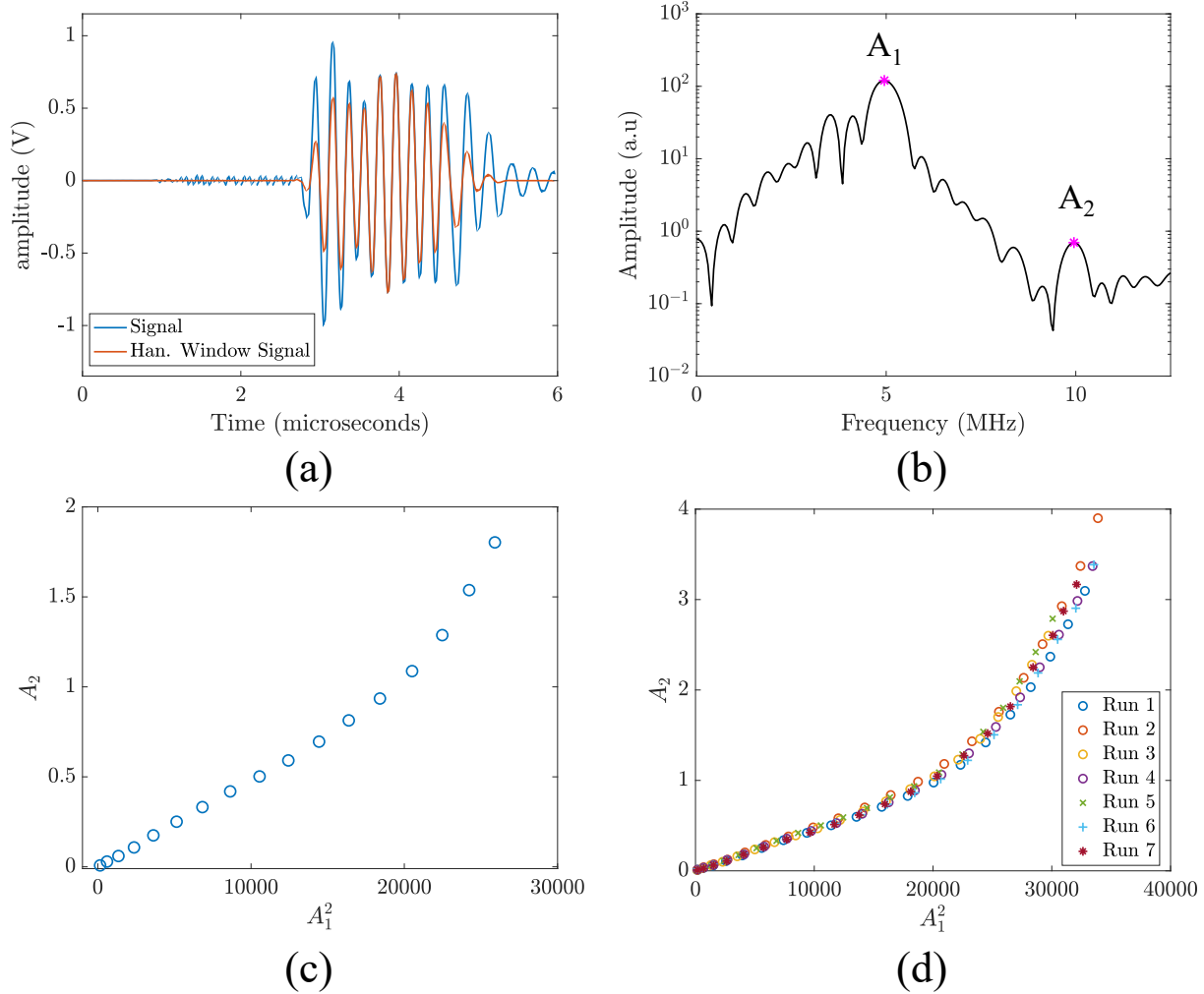


Figure 4-6: Examples of the data analysis steps for SHG testing. These measurements are from plate W-1100-3. The Hann window plotted with the original signal is shown in (a). The frequency spectrum of the windowed signal is shown in (b). Peaks  $A_1$  and  $A_2$  are marked. The evolution of  $A_2$  vs.  $A_1^2$  for the 20 increasing amplitudes is shown in (c). The repeatability results of seven independent tests at the same location are shown in (d).

It can be observed in Figures 4-6c and 4-6d that the entirety of the  $A_2$  versus  $A_1^2$  response does not maintain a linear slope. At the right of the figure, several points representing the highest amplitudes of excitation deviate from the trend. Careful consideration has to be taken during analysis to remove these points from the  $\beta'$  estimation, as they introduce unwanted error

into the final result by increasing  $\beta'$ . The cause of this increased nonlinearity is often attributed to source nonlinearities, such as those introduced by the acquisition system [29].

To establish a quantitative method to remove these points from the data analysis process, the following equation can be generated by taking the relationship between  $A_2$  versus  $A_1^2$  that defines  $\beta'$  (Equation 7), letting an arbitrary value  $n$  replace the quadratic factor on  $A_1$ , and taking the logarithm of both sides:

$$\log_{10} A_2 = n \log_{10} A_1 + \log_{10} \beta^* . \quad (10)$$

From this result, a plot of  $A_2$  vs.  $A_1$  with a logarithmic scale will have a slope of  $n$ . If the slope of the data plotted in this format differs from 2 (from the quadratic relationship governing the theory), further analysis is conducted to adjust the range of data analyzed to assure a nearly-quadratic relationship between  $A_2$  vs.  $A_1$  for the proper estimation of  $\beta'$ . For the linear fit of the data, a minimum  $R^2$  value of 0.98 was desired for a reportable result. The importance of reviewing the SHG data is also observed in literature, such as the Rayleigh wave measurements by Torello et al. [39], although they do not mention any quantitative method for identifying the proper region.

For the example of the analysis process on plate W-1100-3 shown in this section, Figure 4-7a and 4-7b show the fit of the logarithmic graph before and after the optimum range is selected.

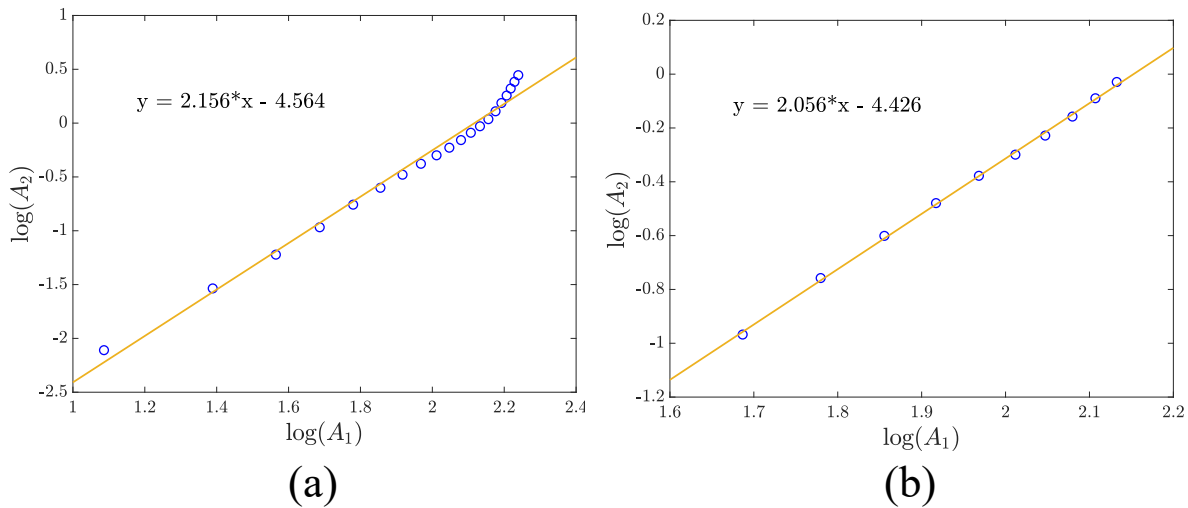


Figure 4-7: A representation of the change in the exponential relationship  $n$  between  $A_2$  and  $A_1$ . **(a)** Shows the result for the entire range of 20 amplitudes, while **(b)** demonstrates the change in slope from the removal of the highest amplitude data points. This data shown corresponds to sample W-1100-3.

After the final estimation of  $\beta'$  for each of the seven runs, the five most repeatable measurements are averaged and reported for each location. This is then repeated for the three locations are each plate. In Chapter 6, the average of the three locations with standard deviations is reported for each plate.

### Pulse-Echo Data Analysis

Pulse-echo data was analyzed for wave speed through a comparison of the arrival times between reflections in the received signal. Because the thickness of the sample is known, by comparing the time of flight in between the first and second arrival of the reflections, the velocity can be estimated.

In MATLAB, the time in between reflections was computed using the technique of cross-correlation. An example of a received pulse-echo signal showing multiple reflections is shown in Figure 4-8. The initial “front wall” of the signal is not considered for analysis. Rather, the arrival time of the back surface reflections is measured. The cross-correlation function compares the similarity of the back surface reflections as a function of their relative phase to one another. The back surface reflections do not become distorted as they propagate, but their amplitudes decay exponentially. For this reason, their shapes can be compared. When the cross-correlation is at its maximum value, this indicates the waves are most directly overlapping, and the phase difference between them is used to calculate the time-of-flight. Dividing the total distance traveled by the wave (for the first two back surface reflections, this is double the sample thickness) by the time-of-flight gives the estimation of the wave speed.

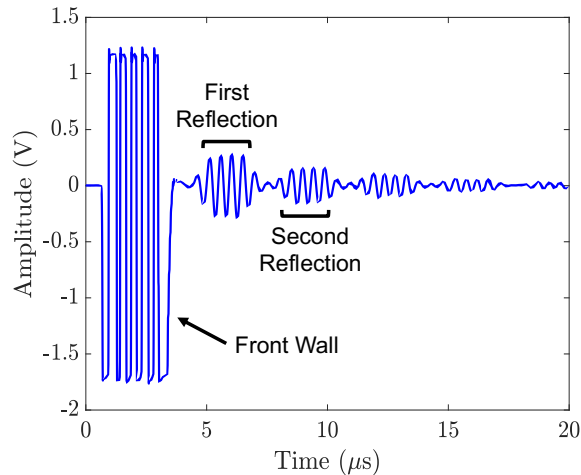


Figure 4-8: An example of a received pulse-echo signal.

In these experiments, three pulse-echo tests were conducted for each sample according to the previously described testing protocols. The results shown in Chapter 6 represent the mean and standard deviation of these tests for each plate.

## Chapter 5

### Results of Numerical Modeling

The results of numerical modeling will be assessed through parametric studies of the heterogeneous model. After the validation studies presented in Chapter 3, the remaining simulations contain heterogeneities with assigned properties that differ from the bulk plate.

Several constraints have been imposed on these numerical experiments. The radius of each particle is held constant, and each particle is modeled as a circle. When studying changes in particle size, volume fraction will be held constant, therefore reducing the number of particles with increasing radius. Future studies will explore scripting elliptical and randomly distributed particle radii as additional forms of heterogeneity.

Table 5-1 shows two different properties chosen for the heterogeneities with different objectives. “Study 1” intends to match the impedance of the bulk material and heterogeneities while maximizing the difference in their wave speeds. “Study 2” achieves the opposite, matching wave speeds while maximizing the difference in impedance. Compared to the bulk material, Study 1 offers a 51% decrease in density and 37% decrease in elastic modulus. For Study 2, these values are 77% and 93%, respectively.

Table 5-1: Material properties of the distributed heterogeneities in each study

	Density (kg/m <sup>3</sup> )	E (GPa)	G (GPa)	$\nu$
Bulk Material	7,800	210.38	82.39	0.277
Study 1	3,802 (-51%)	133.00 (-37%)	52.08	0.277
Study 2	1,800 (-77%)	14.96 (-93%)	5.858	0.277

## The Effect of Incident Amplitude on Higher Harmonic Generation

The first amplitude study involves distributing particles throughout the plate but keeping their material properties identical to the bulk. This results in a plate with distributed particles, although its overall material is homogeneous. The particle radii are 50  $\mu\text{m}$ , with a 7.5% volume fraction. The microstructure is unchanged in between tests, while the amplitude is varied incrementally between 0.1 and 5  $\mu\text{m}$ . Because the plate has no actual heterogeneity, despite having distributed particles, no HHG should be observed at any amplitude. The results in Figure 5-1 confirm this hypothesis.

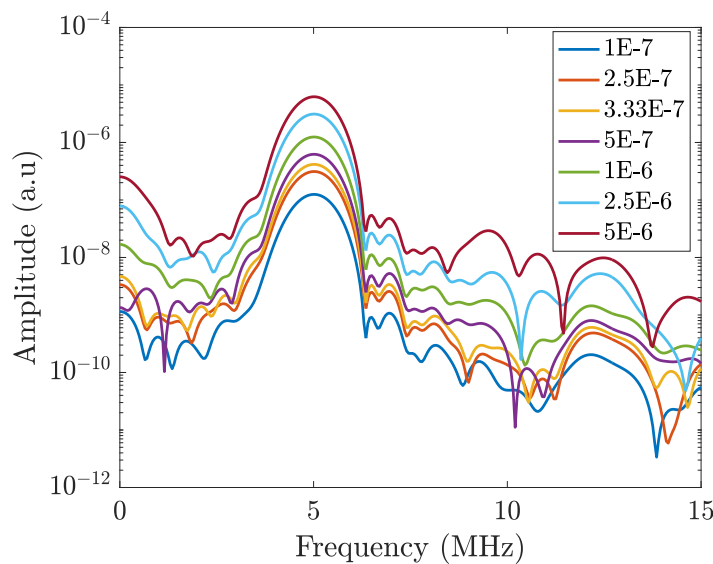


Figure 5-1: Amplitude study on a plate with distributed heterogeneities with properties matching the bulk material. Observe no HHG at 10 MHz.

The first simulation conducted with a truly heterogeneous model aims to explore the effects of the incident amplitude on wave distortion and HHG. The obtained results are shown in Figures 5-2a and 5-2b. Study 1 properties are chosen for the heterogeneities at a volume fraction of 7.5%, with the same distribution used in the model that was just discussed (Figure 5-1). Only

the material properties of the heterogeneities are changed. It is observed that  $A_2$  is linear to  $A_1^2$  for monotonously increasing incident amplitudes, and higher harmonics are generated at 10 MHz. Note this result was also confirmed with different volume fractions of particles, as well as the material properties of Study 2. These results are in agreement with the analytical model of Li et al. [27].

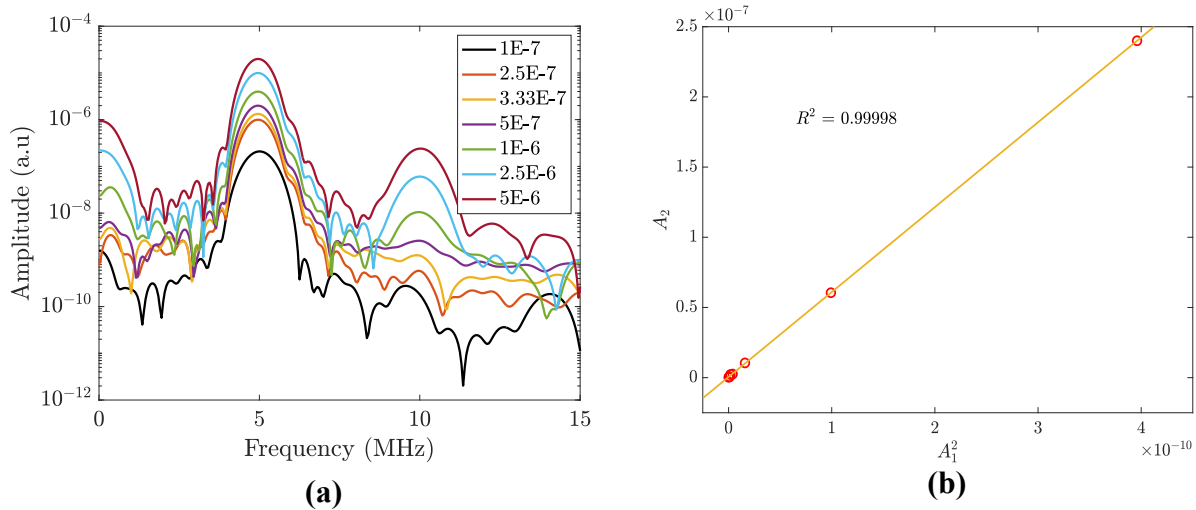


Figure 5-2:  $A_2$  vs.  $A_1^2$  where incident amplitude varies from 1E-7 to 5E-6. (a) The FFT for each increasing amplitude. (b) The ratio of second harmonic peak  $A_2$  to fundamental  $A_1^2$ .

The presence of HHG in Figure 5-2 and the lack of HHG in Figure 5-1 suggests the heterogeneities influence on wave distortion for this linear elastic model. The next studies will focus on varying the size, volume fraction, and material properties of these distributed heterogeneities. In all the following results, an incident amplitude of 1E-6 is chosen, the third-largest used in this study.

### The Effects of Particle Size on Higher Harmonic Generation

The sole presence of precipitates or second-phase particles within a microstructure has not been attributed to significantly altering the magnitude of  $\beta$  during nonlinear ultrasonic testing [40]. However, their interactions with other features in the surrounding matrix, such as dislocations, have been shown to offer significant contributions to HHG [11].

To study the influence of particle size on wave distortion, heterogeneities with radii ranging from 40 – 120  $\mu\text{m}$  at a constant volume fraction of 5% were simulated. The results of this process are shown in Figure 5-3 for HHG (5-3a) and wave speed (5-3b) with material properties of Study 1 and 2. Note that when comparing the results of the two studies for the same particle radii, the mesh was not regenerated i.e., only the material is altered.

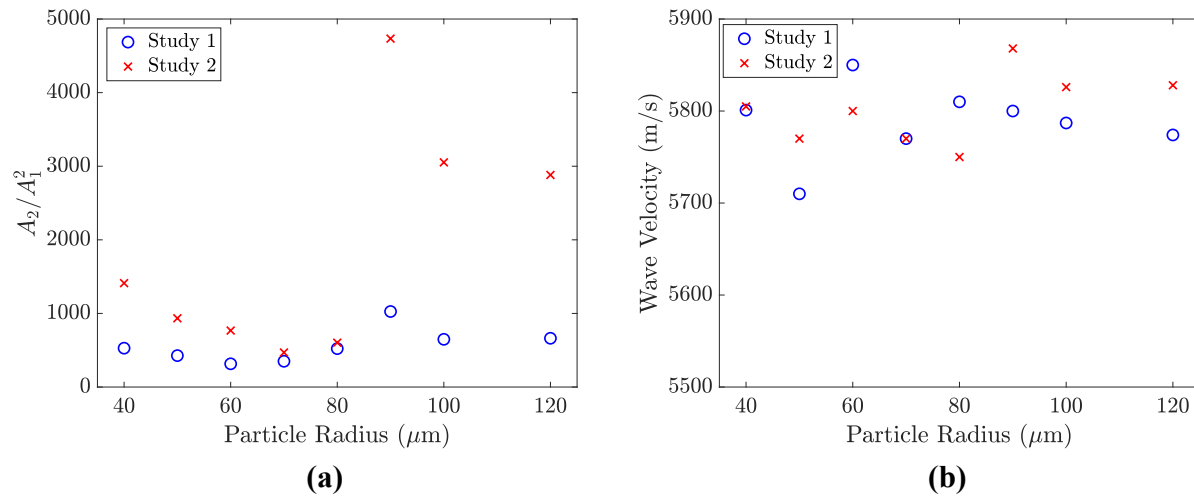


Figure 5-3: The influence of particle radius on wave distortion for material properties of Study 1 and Study 2. **(a)** Changes in wave distortion ( $A_2/A_1^2$ ), and **(b)** wave velocity.

Results for both studies generally follow the same trend. A decreasing amount of HHG is observed for increasing radii between 40 and 70  $\mu\text{m}$ . The trend then reverses with a jump at 90

$\mu\text{m}$ , the largest magnitude in both studies. Further increases in radii result in a decrease in magnitude. In every case, Study 2 resulted in a higher level of wave distortion than Study 1. Also, sizes on the order of  $100 \mu\text{m}$  consistently result in increased HHG than those on the order of  $10 \mu\text{m}$ . The effect of particle size on HHG was also observed by Kamali et al. [23] and Li et al. [27], with further discussion in Chapter 7.

Wave speed shows no significant changes with particle radius, varying within a 1.5% range between 5700 and 5850 m/s. This observation in wave speed is consistent with expectations, because although the size of the particle is changing, the volume fraction is held constant. Therefore, the overall composition of the material, and therefore its wave speed, should not change with particle size.

### **The Effects of Particle Volume Fraction on Higher Harmonic Generation**

Next, an investigation into the effects of the volume fraction of heterogeneities is considered. Particle size was held constant at  $90 \mu\text{m}$  and the volume fraction was varied between 1% and 10% in steps of 2%. This size was chosen because it resulted in the maximum amount of HHG in the previous investigation. Figure 5-4 shows these results for wave distortion (5-4a) and velocity (5-4b). Once again, the distribution of heterogeneities (mesh) was not altered between Study 1 and Study 2 of the same volume fraction.

The results of Study 1 indicate a higher sensitivity to particle size, with a significant increase at volume fractions between 5% and 10%. At volume fractions below 5%, the results of Study 1 and 2 have similar decreasing trends. Higher volume fractions result in little change in Study 2. Wave velocities are largely unchanged for both material properties, with Study 2

consistently having a slightly larger wave velocity than Study 1. These velocity values stay within a 0.5% range between 5,790 and 5,840 m/s.

In contrast to the study of particle size on wave speed, these results do not follow our hypothesis. With the increasing volume fraction of particles, it is expected that the wave speed will change. For example, a simulation run with a fully homogeneous plate with Study 2 material resulted in a wave speed of approximately 2,900 m/s, while the wave speed of the homogeneous bulk plate is approximately 6,000 m/s. At increasing volume fractions of Study 2 particles, a reduction in wave speed is predicted. However, the results do not indicate this. A potential explanation is that the wave may not experience a totally accurate volume fraction of heterogeneities during its travel, because the incident wave does not interrogate the entirety of the plate and the heterogeneities are not uniformly distributed.

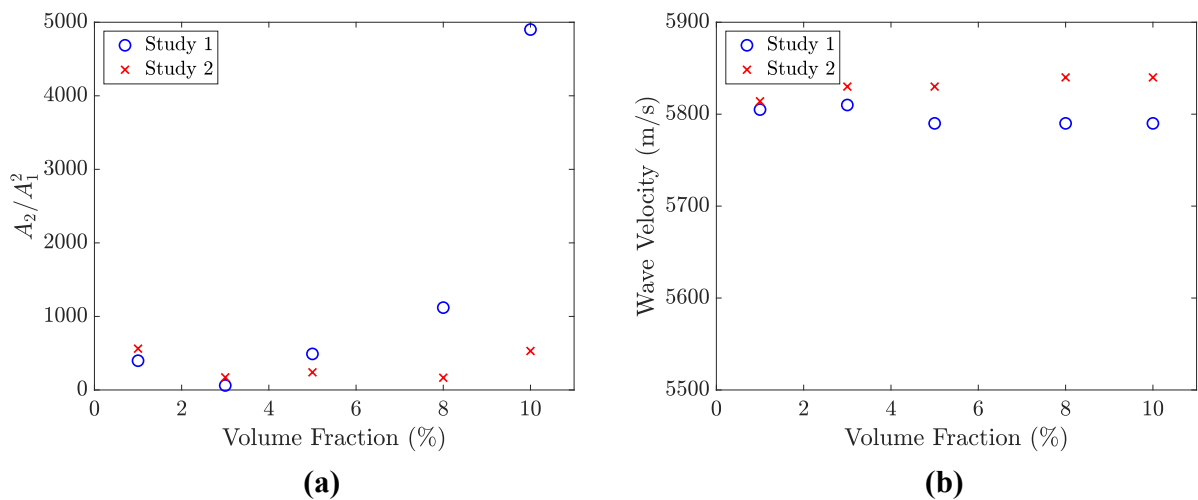


Figure 5-4: The influence of volume fraction of heterogeneities on wave distortion for material properties of Study 1 and Study 2. **(a)** Changes in HHG ( $A_2/A_1^2$ ), and **(b)** wave velocity.

Although our simulations use linear elastic material models, these results are in agreement with those of Kamali et al. [23] in their numerical study of Aluminum 1100 with

distributed defects. They note that at small volume fractions (1%) and heterogeneity sizes (80  $\mu\text{m}$ ), the “strength deviation,” or difference in Elastic Moduli between the bulk and the heterogeneities, has little influence on the HHG. However, with increasingly larger heterogeneity sizes that are of the mesoscale (230 and 640  $\mu\text{m}$ ) and larger volume fractions (10% and 20%), the influence of strength deviation results in HHG increases as much as 50%. In our results, a significant increase is also observed with sizes over 100  $\mu\text{m}$  and volume fraction approaching 10%.

## Chapter 6

### Experimental Results

The results of the laboratory experiments will be presented in three sections: the first section will show the results of tensile testing. The second section will share the results of linear and nonlinear ultrasonic testing. Finally, the third section will combine the mechanical and ultrasonic testing data for the goal of correlating ultrasonic response to mechanical properties.

#### Results of Mechanical Testing

Figure 6-1a shows the UTS response for each manufacturing method and heat treatment of 316L samples. In the wrought samples, initial heat treating to 600 °C provided an increase in UTS when compared to the as-built condition. Transmission electron microscopy (TEM) shows as-built AM steel contains a much higher density of dislocations compared to wrought and annealed steel microstructures, which is in agreement with our results [41]. The as-built strength of AM 316L measured in these experiments is consistent with review values [38]. Continued heat treating at higher temperatures resulted in a gradual decline in strength. For AM components, the heat treatment process resulted in reduced UTS across increasing heat treatment temperatures, with the highest strength in the as-built sample.

In a review of L-PBF, Ladani and Sadeghilaridjani compare the as-built strengths of wrought and L-PBF AM 316L components, where AM samples have considerably larger strengths. In one study, up to a 34% increase in UTS is reported between wrought and AM 316L stainless steel. Explanations include the formation of nano-inclusions in the AM parts that hinder dislocation movement, as well as a large density of low-angle grain boundaries [42].

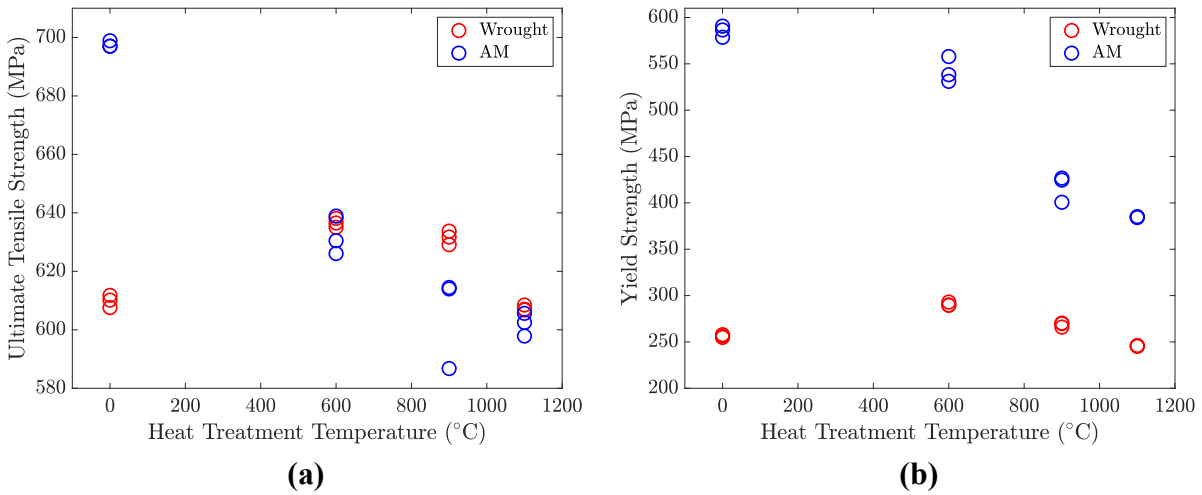


Figure 6-1: The results of mechanical testing on both wrought and AM components: **(a)** Ultimate Tensile Strength, and **(b)** Yield Strength.

The results for YS are shown in Figure 6-1b. Similar to UTS, YS in wrought components show an initial increase at the 600 °C heat treatment when compared to the as-built samples. For higher temperature heat treatments, YS declines. In AM samples, the as-built components show the highest YS, which then declines for each increasing heat treatment temperature. Similar to UTS, as-built YS values in AM 316L stainless steel are reported as much as double that of wrought [42], [43]. It can be observed that in both YS and UTS, the mechanical properties of wrought and AM samples start to converge with increasing heat treatment.

Figure 6-2a displays results for the Elastic Moduli. While the data displays more variability than the parameters in Figure 6-1, it can be observed that the Elastic Moduli of AM components is generally greater than in the wrought samples. Increasing heat treatment temperatures also offers a minor increase in the Elastic Moduli for AM components. No clear trends are present for wrought components, which display higher variability.

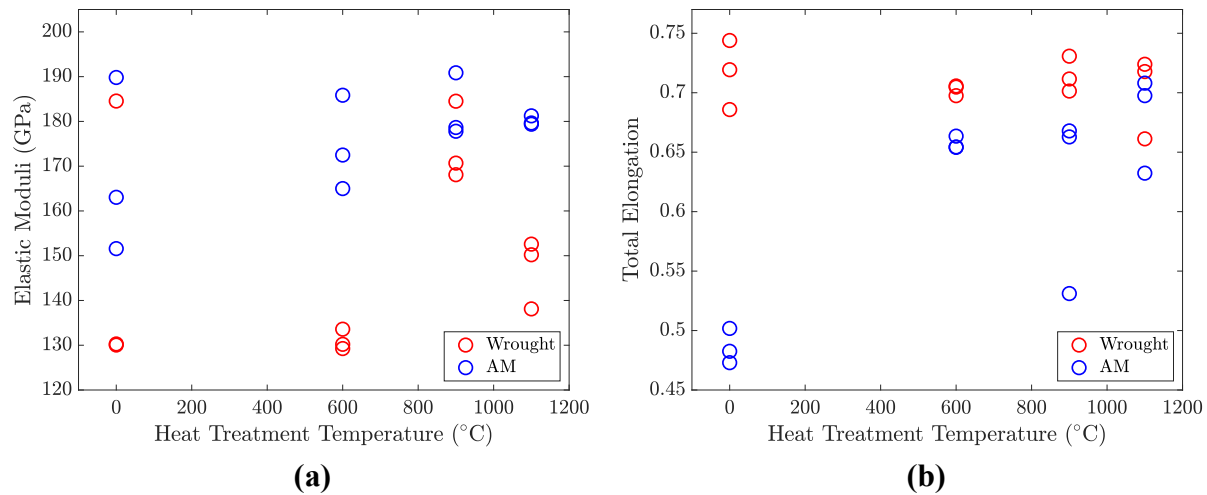


Figure 6-2: The results of mechanical testing on both wrought and AM components: **(a)** Elastic Moduli, and **(b)** Total Elongation.

Finally, total elongation results are shown in Figure 6-2b. For the wrought components, no trend is discernable between total elongation and heat treatment. However, for AM samples, heat treatment results in a notable increase in total elongation when compared to the as-built plates, which is in agreement with literature [38]. For elongation, one can again observe that with increases in heat treatment, the behavior of wrought and AM samples becomes more similar.

Reduced ductility is often attributed to the presence of porosity, which is randomly distributed through a microstructure. High amounts of variation in elongation for samples of the same heat treatment are attributed to the randomness of pore orientation, specifically relative to the loading direction of the tensile test. The maximum stress concentration, which represents the orientation with the lowest energy necessary to initiate void growth, occurs where the loading is applied normal to the major axis of the pore [43]. Using x-ray tomography, du Plessis et al. [44] observed that L-PBF components often contain small amounts of multiscale porosity, depending on processing parameters such as laser power or scan speed. Despite this, they concluded that for

low volume fractions (~1%), porosity contributed minimally to mechanical behavior in comparison to surface roughness or geometry. Further, they attribute the lack of fusion defects as more detrimental, which can be prevented through smaller layer thickness and increased laser power.

### Results of Ultrasonic Testing

Following the data collection and analysis protocols described in Chapter 4, results of both linear and nonlinear ultrasonic parameters are presented in this section. In Figure 6-3a, each data point is the average  $\beta'$  value of the five most repeatable SHG tests conducted on each plate. The error bars represent  $\pm 1$  standard deviations of these five averages. This figure enables a more detailed perspective of the error associated with the SHG testing of each sample, where overall trends are difficult to visualize.

For wrought samples, the plate numbers were chosen arbitrarily upon the collection of the samples before SHG testing. The numbers on each AM sample correspond to the build plate location during the manufacturing process. However, these samples were printed on the same build, and only heat treatment differentiates them.

For these reasons, more condensed results of SHG testing are shown in Figure 6-3b. For each heat treatment, the data point represents the global average of each plate result shown in Figure 6-3a. Error bars represent  $\pm 1$  standard deviation of these local averages. Here, the response of wrought components shows little trend across each heat treatment. For AM components, a general increase in  $\beta'$  is present as heat treatment temperatures increase. This trend was reported elsewhere in literature, such as an increase in bulk wave measurements of  $\beta'$

with 1 hr heat treatment of aluminum alloy samples was reported by Kim and Jhang [45].

Additional details can be found in Chapter 7. It can also be noted that the as-built AM samples have considerably lower variation than the heat-treated AM samples.

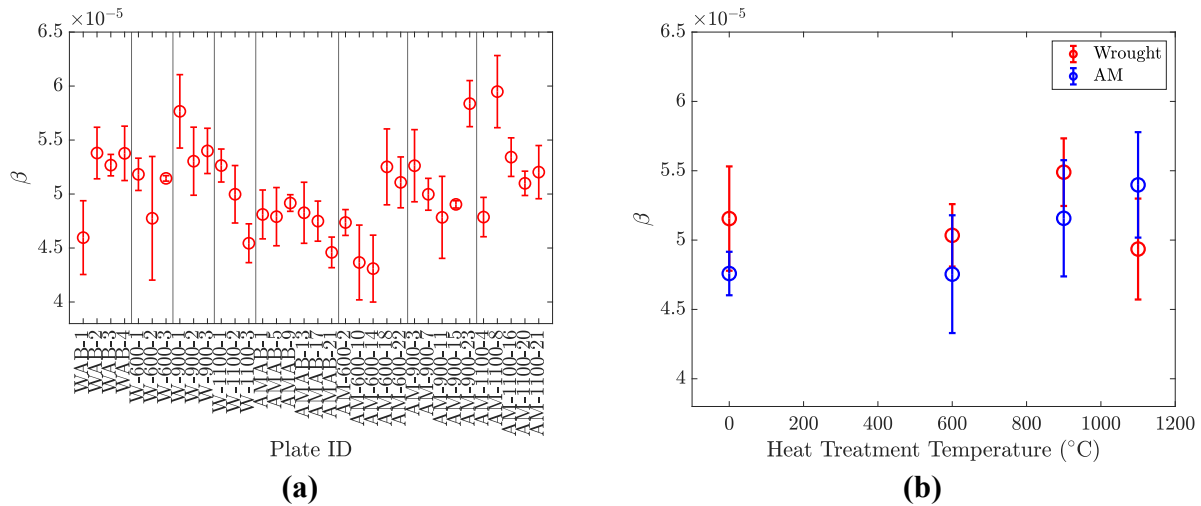


Figure 6-3: The results of nonlinear SHG testing on both wrought and AM components: (a) Detailed individual plate results, and (b) overall results for each heat treatment.

Figure 6-4 displays the results for the linear ultrasonic parameter, wave speed. For wrought samples, the trend in wave speed appears to follow trends in UTS and YS, where there is an initial increase between as-built samples at the first heat treatment, followed by a gradual decrease through higher temperatures. It can be observed that the wave velocities of the AM samples show little variations across heat treatments.

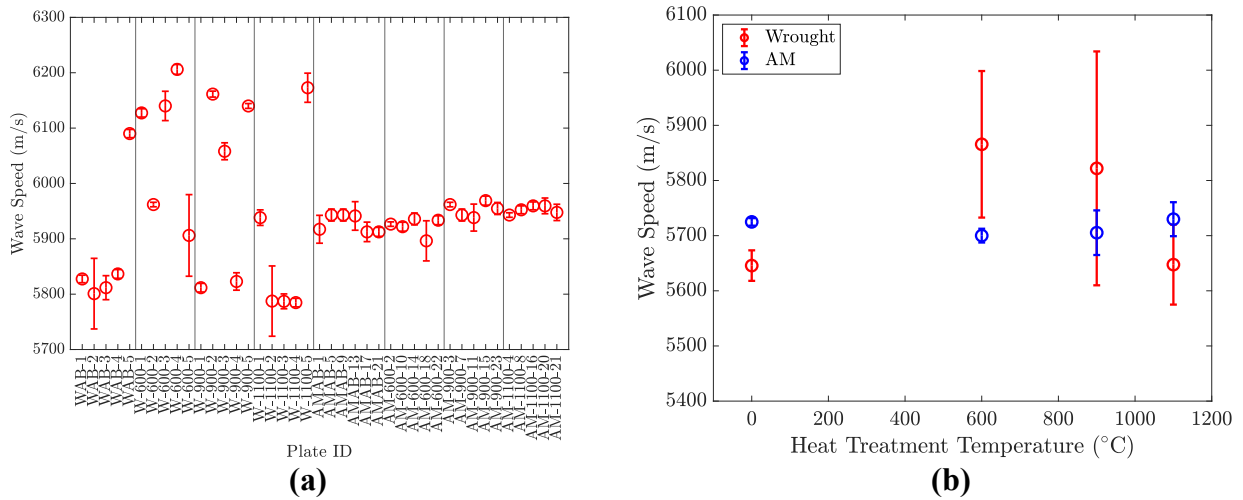


Figure 6-4: The results of linear pulse-echo testing on both wrought and AM components: **(a)** Detailed plate results, and **(b)** overall results for each heat treatment.

Variability in wave speed of the wrought samples is significantly larger than AM. For the wrought as-built (WAB) samples, the wave velocity of WAB-5 was an outlier relative to the remaining four WAB samples, and was removed. Similarly, W-1100-5 was also removed from the final data. Potential explanations for these outliers in the wrought samples could be attributed to the rougher surface finish present in a small number of wrought samples.

### **Relationships Between Ultrasonic and Mechanical Parameters**

For each of the parameters measured during the mechanical testing, results are plotted here alongside both linear and nonlinear ultrasonic parameters. For readability, the combined ultrasonic data for each heat treatment (Figures **6-3b** and **6-4b**) is plotted. Figures **6-5** - **6-8** plot the relationships between linear and nonlinear ultrasonic parameters and the four mechanical parameters measured for each sample, separated by the manufacturing method.

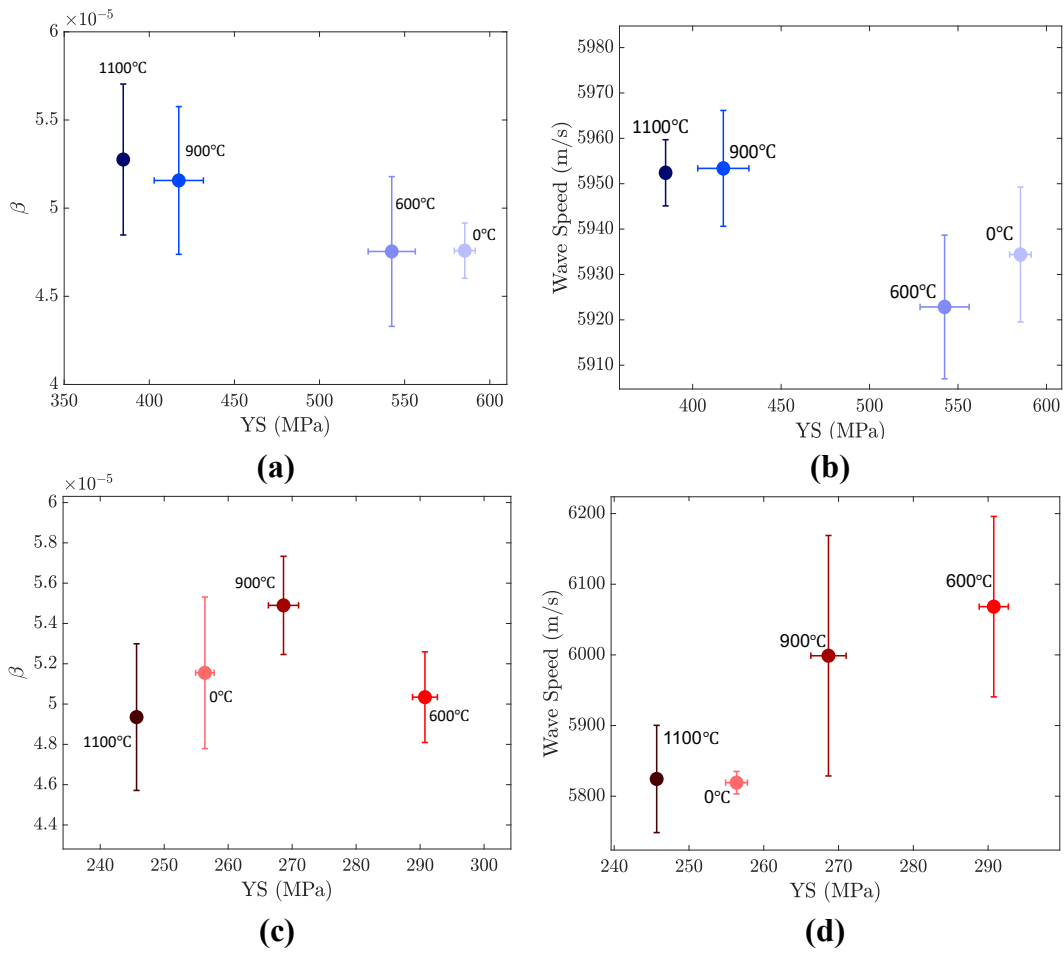
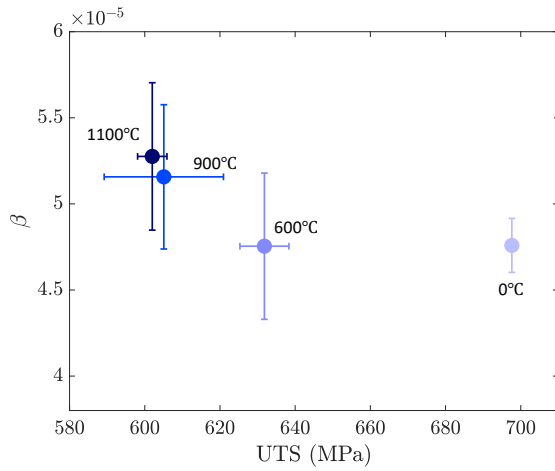
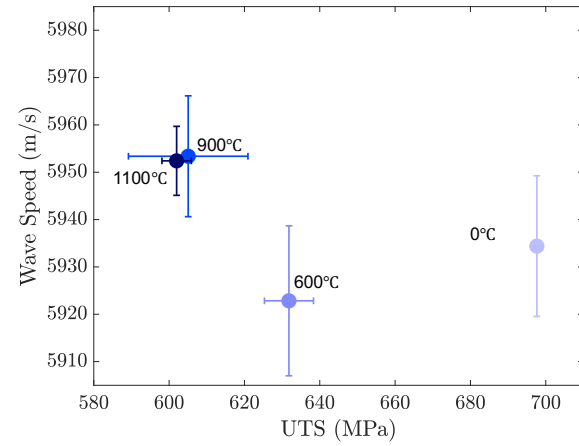


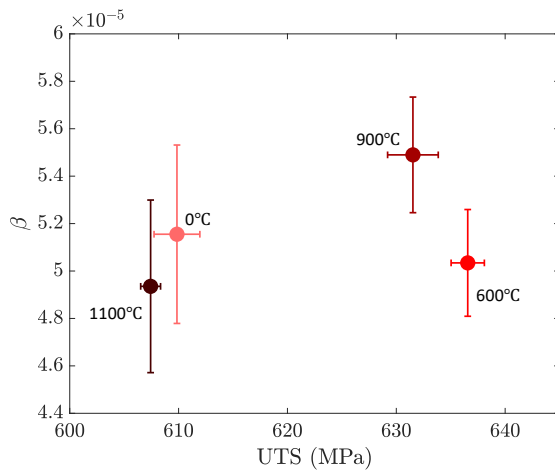
Figure 6-5: Combined results of YS and ultrasonic testing: (a) YS plotted against the nonlinearity parameter  $\beta'$  in AM samples, and (b) linear wave speed in AM samples. (c) and (d) show the results of  $\beta'$  and wave speed for wrought samples.



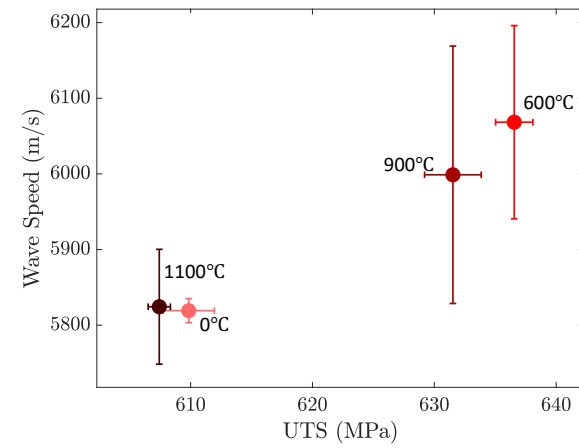
(a)



(b)



(c)



(d)

Figure 6-6: Combined results of UTS and ultrasonic testing: (a) UTS plotted against the nonlinearity parameter  $\beta'$  in AM samples, and (b) linear wave speed in AM samples. (c) and (d) show the results of  $\beta'$  and wave speed for wrought samples.

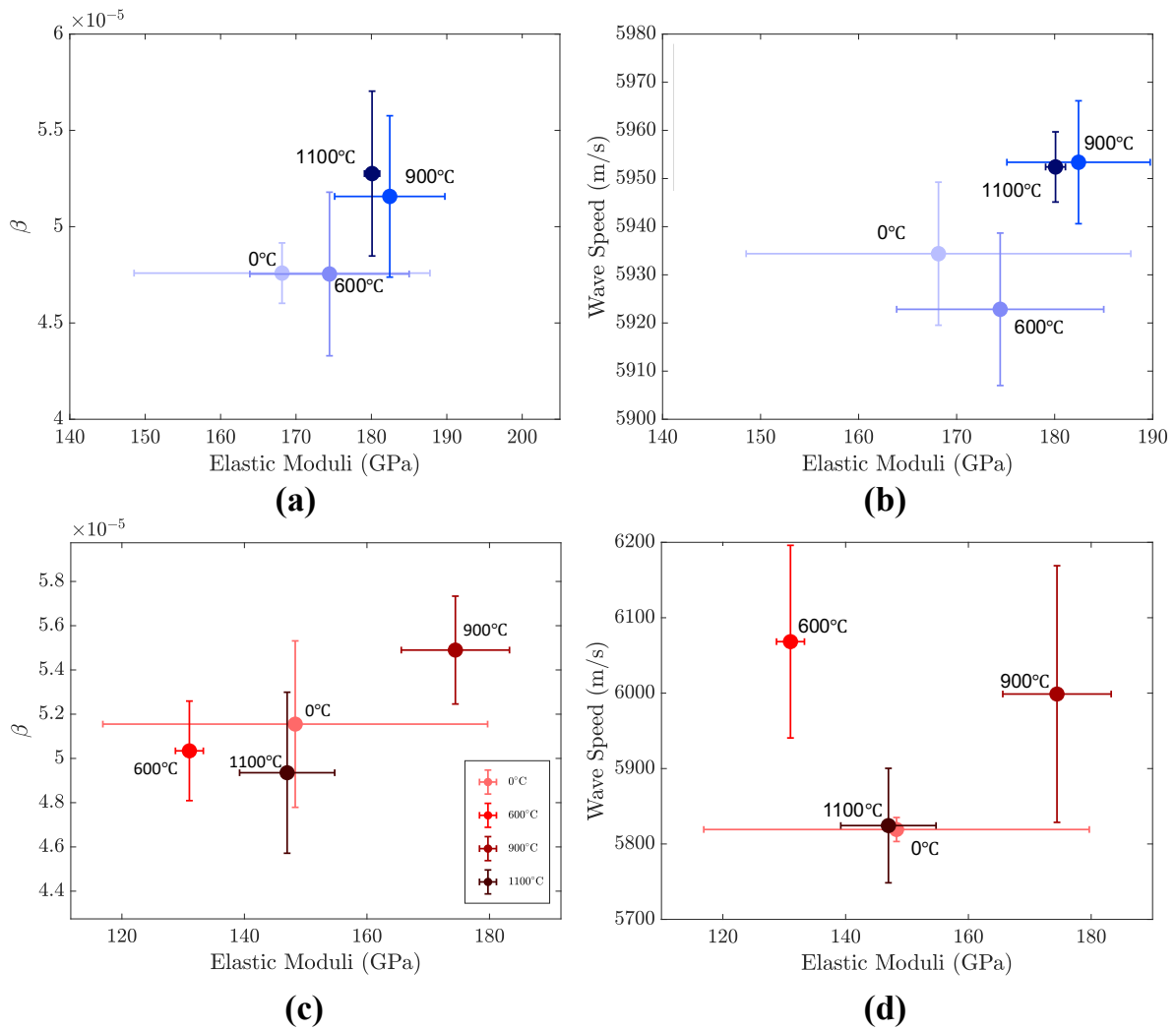


Figure 6-7: Combined results of Elastic Moduli and ultrasonic testing: **(a)** Elastic Moduli plotted against the nonlinearity parameter  $\beta'$  in AM samples, and **(b)** linear wave speed in AM samples. **(c)** and **(d)** show the results of  $\beta'$  and wave speed for wrought samples.

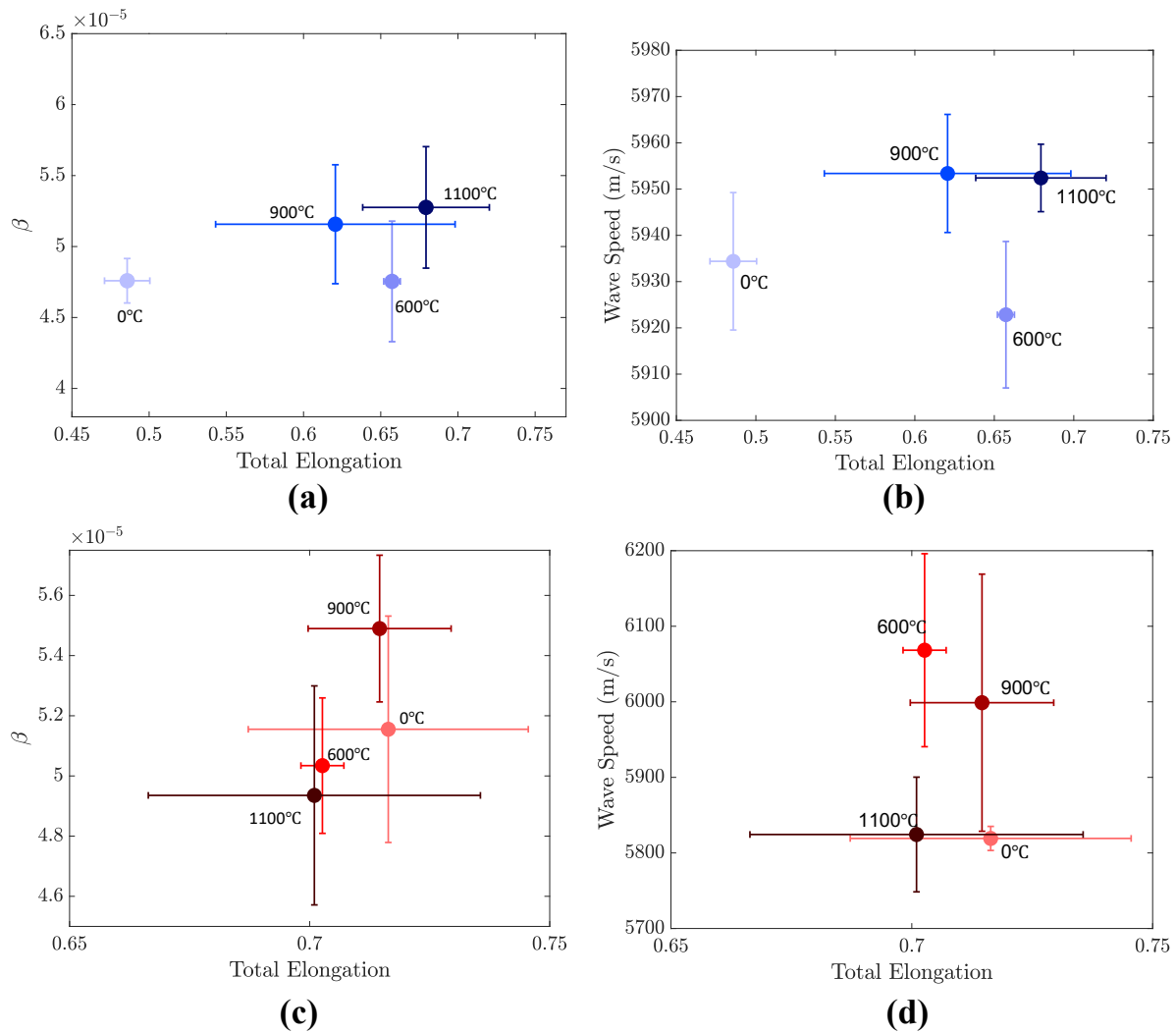


Figure 6-8: Combined results of total elongation and ultrasonic testing: (a) Total elongation plotted against the nonlinearity parameter  $\beta'$  in AM samples, and (b) linear wave speed in AM samples. (c) and (d) show the results of  $\beta'$  and wave speed for wrought samples.

Observations of results for the strength properties (Figures 6-5 and 6-6) show that higher  $\beta'$  measurements correspond with reductions in strength. This could be attributed to a higher concentration of defects, which would increase the nonlinearity of the material. Further, both results show trends with heat treatment in AM parts. The 1100 °C heat treatment sample has the highest  $\beta'$  and lowest strength, and proceeds from left to right in order of decreasing heat

treatment temperature. Results for Elastic Moduli (Figure 6-7) indicate that AM components generally have a larger value than wrought. Finally, it can be observed in Figure 6-8 that heat treatment increases fracture elongation, particularly in AM components. In any of these four results, linear wave velocity does not show significant trends with mechanical properties in AM parts. In AM samples, UTS and YS (Figures 6-5b and 6-6b) wave speed results are grouped into two higher and two lower heat treatment temperatures, with the higher temperature plates having slightly larger wave speeds.

## Chapter 7

### Discussion

When considering the linear and nonlinear ultrasonic responses for each plate tested, we observe that the process of heat treatment has effects on the nonlinearity parameter ( $\beta'$ ) of wrought and AM samples, albeit in different ways. While the nonlinearity and mechanical properties do not vary as significantly in heat-treated wrought samples, both YS and UTS show trends with  $\beta'$  in AM components, where higher values of  $\beta'$  are observed at lower YS and UTS.

One significant observation is the lack of discernable trends in the wave speed and mechanical properties of AM samples. For UTS and YS, a slight increase in wave speed is observed for the two higher temperature heat treatment AM parts. The wavelength of the emitted 5 MHz pulses used in this study was approximately 1 mm, which is considerably larger than many of the microscale features influencing the mechanical properties. This result further reinforces the necessity of nonlinear ultrasonic parameters for assessing microscale and sub-micron material evolution, which is not achievable using less microstructure-sensitive linear methods.

In wrought samples, a relationship exists between the trends in strength properties (UTS and YS) and wave speeds with heat treatment. Higher wave speeds are often attributed to decreased porosity and improved mechanical properties. This observation is supported by results in wrought components, where the largest wave speed, YS, and UTS all occur at the same sample (600 °C) and gradually decrease together with increasing heat treatment temperatures.

Increases in  $\beta'$  with higher heat treatment temperatures were reported by Kim and Jhang on an aluminum alloy [45]. The sample thickness was 20 mm, and the frequency of the incident wave was 5 MHz. The heat treatment temperatures used were 250, 300, and 350 °C. The ultrasonic and tensile tests were conducted periodically between 0 and 50 hr of heat treatment for each temperature. At the 1 hr interval, an increase in  $\beta'$  was reported in every heat treatment with respect to the as-built samples, with the highest  $\beta'$  value measured in the sample with the highest heat treatment temperature. Although using different materials and temperatures during heat treatment, these results are in agreement with the results of our bulk wave study of AM samples at 1 hr heat treatment time. Further, the lowest YS is measured in the aluminum alloy sample with the highest heat treatment temperature and highest value of  $\beta'$ , in agreement with our observations for AM samples. Additionally, the linear elastic constant (elastic moduli) did not show any appreciable changes with heat treatment time or temperature in these experiments. This is in agreement with our results for both wrought and AM components.

In another study, Williams et al. reported increasing values of  $\beta'$  with increasing heat treatment temperature in 4130 steel samples measured with bulk wave SHG testing [19]. These samples were 10 mm thick and heat-treated for 2 hr with temperatures ranging between 150 and 663 °C. Surface wave measurements were also conducted on these plates, and the results showed a different trend. The highest value of surface wave  $\beta'$  was measured at the lowest heat treatment temperature, which then decreased in a nearly monotonic trend with increasing heat treatment temperature. A slight reversal and increase in  $\beta'$  was then observed for the two highest heat treatment samples. Differences between bulk and surface wave measurements of  $\beta'$  are an area of interest for future study, and hypotheses include the difference in wave motion between bulk

and surface waves, and different depths of heterogeneous material being interrogated by the surface and bulk wave modes, respectively.

The surface wave measurements conducted on 316L L-PBF samples with similar heat treatments from Bellotti et al. showed a trend where  $\beta'$  decreased linearly with increasing heat treatments between 650 and 1050 °C, with a reversing increase in  $\beta'$  at the highest treatment (1200 °C) [31]. This trend was attributed to a reduced dislocation density at increasing heat treatments and confirmed with analysis using electron backscatter diffraction (EBSD). EBSD was used to measure geometrically necessary dislocations, a quantitative indicator of dislocation density. These results do not corroborate those in our study, however, differences in processing and experimental parameters should be noted. As noted above, differences between trends in  $\beta'$  measured using bulk wave and surface wave testing are reported by Williams et al. which could also explain the discrepancy between these two studies. As opposed to bulk wave SHG, surface wave tests only interrogate a depth of approximately  $1-1.5\lambda$  into the material, or approximately 1.5 mm from the reported 2.1 MHz incident wave. All samples in our study were treated for 1 hr, while the three lower heat treatment samples in [31] were heat-treated for 0.5 hr, and the 1200 °C sample was treated for 2.5 hr. Regarding the processing parameters in L-PBF, laser power in our study was 107% larger (214 W vs 103 W), and our scanning speed was 34% slower (928 mm/s vs 1400 mm/s).

Such differences in processing parameters have been shown to dramatically alter AM material properties and microstructure. Jaskari et al. [46] studied L-PBF 316L, concluding that changing volume energy density (related to the ratio of laser power to scan speed) results in changes in melt pool width, grain size, material density, elongation behavior, and defect size. Comparing our study to [31], there is an increase of more than 200% between ratios of laser

power to scan speed. In the comparisons of Jaskari et al, there is only a 66% increase between the “low” and “high” energy densities that result in significant observed microstructural changes. This implies that there are likely notable microstructural differences between the 316L samples of Bellotti and our study, which may explain the different observed trends. This possibility will be investigated through optical and electron microscopy of our samples.

Trends in the strength of L-PBF 316L components are well documented in literature. Ronneberg et al. [43] used both optical and electron microscopy to analyze the microstructural evolution of L-PBF 316L components from 1 hr heat treatments between 700 and 1200 °C. Optical microscopy at a 100  $\mu\text{m}$  length scale detected no microstructural differences for heat treatments between 700 and 1040 °C. Only at 1200 °C were grain growth and the presence of annealing twins noticeable. SEM at a 5  $\mu\text{m}$  resolution allowed for more distinction between the samples. Even at a higher resolution, no differences were observed between as-built and 700 °C samples. Our nonlinear results are in agreement with these reported observations indicating nearly equal  $\beta'$  values for as-built and 600 °C AM samples. Despite this, the differences in YS and UTS between them suggest decreases in dislocation density with heat treatment, in agreement with dislocation studies of Bellotti et al. [31]. In the heat treatment range of 700 – 1040 °C, atomic diffusion is initiated, which dissolves grain and melt pool boundaries, attributing to reductions in YS and UTS seen in our study as well as other results ([43], [46]). The general improvement in strength between wrought and as-built L-PBF parts is also well documented and attributed to multiple sources in AM components including finer sub-grains, higher dislocation density, and nanometer-scale precipitates [41]–[43], [46].

Finite element simulations studied the interactions between randomly distributed heterogeneities and wave distortion in a linear elastic medium. Results indicate observable

changes in HHG for different heterogeneity inclusions, geometries, and volume fractions.

Although a linear elastic material model is used, the ratio of generated second harmonic relative to incident amplitudes is consistent with the numerical and analytical results reported in literature ([23], [27]) as well as experimental studies and theory of SHG. These results are surprising and need further investigation.

The differences between the amplitude studies of the homogeneous and heterogeneous plate suggest that the presence of heterogeneities with differing material density and stiffness have a contribution to wave distortion and HHG. The homogeneous model provides a baseline for comparison. Future work will aim to understand this phenomenon, as well as continue to run additional simulations with different parameters while investigating the variability in the results when repeatedly generating new microstructural distributions.

Changes in HHG as a function of particle size were reported in the analytical model of Li et al., although at a smaller length scale. In those results, larger particle sizes generally increased HHG. Comparing the HHG for particle sizes that approach the mesoscale length ( $\sim 100 \mu\text{m}$ ) agrees with the results of Kamali et al. [23] where particle sizes of 80, 320, and 640  $\mu\text{m}$  are modeled at volume fractions of 1, 10, and 20%.

The volume fraction results are also in agreement with observations of Kamali et al. In contrast to our simulations, a more complex hyper-elastic material model (Landau-Lifshitz) is utilized. Despite this major difference, similar trends between models are captured. For example, both results indicate a significant increase in HHG when comparing particle sizes on the order of  $\sim 10$  and  $\sim 100 \mu\text{m}$ . The capability of a simpler model to capture trends observed in more complex models and physical data is also supported by Van Pamel in their simulations of wave propagation through polycrystalline materials [25].

The next steps of the simulations will include repeating tests with the same parameters with redistributed heterogeneities, to study the influence of variability in the random microstructures on HHG. Also, future simulations will employ nonlinear constitutive models, and repeat the process of studying heterogeneity distributions conducted here with the linear elastic constitutive model. For example, the comparison of studies with linear elastic and nonlinear elastic models with distributed heterogeneities will decouple the influence of the inhomogeneities and the constitutive relationships as they both contribute to HHG. Additional future objectives are discussed in Chapter 8.

## Chapter 8

### Conclusion and Future Work

In this study, linear and nonlinear ultrasonic tests along with tensile properties of 316L stainless steel were investigated for wrought and L-PBF AM samples of varied heat treatments, with the goal to develop an ultrasonic method for quality assurance in AM parts. The linear ultrasonic parameter of wave speed was measured using pulse-echo testing, while the relative nonlinearity parameter  $\beta'$  was measured using SHG. A methodology for creating numerical simulations of distributed microstructural heterogeneities was also studied to understand the effects of randomly distributed heterogeneities on HHG in a controlled environment. Heterogeneity characteristics include size, volume fraction, and material properties relative to the bulk medium. The accuracy of the numerical model was verified through comparisons to homogeneous material, as well as comparing the simulated effects of porosity to experimental and analytical results.

Experimental results indicate relationships between  $\beta'$  and the strength characteristics (YS, UTS) of AM components through a range of heat treatments. AM components also exhibited larger elastic moduli than wrought at the same heat treatments. As the heat treatment temperatures increased, a convergence between the strength properties of AM and wrought components was observable, particularly in UTS, but also for YS and total elongation. The linear ultrasonic parameter of wave speed did not display the capability to distinguish tensile properties in AM parts.

Results of the simulation show that with the presence of heterogeneities, HHG can be measured in the samples using the same incident ultrasonic waves as experimental testing.

Samples with larger sizes (approaching the mesoscale  $\sim 100 \mu\text{m}$ ) and volume fractions (10%) of distributed particles exhibited significant increases in HHG. The deviation in the material density and elastic moduli of the distributed heterogeneities also had a significant influence on HHG, a trend that was accentuated in increasing particle sizes and volume fractions.

The future work for the experimental and numerical portions of this research aims to gradually converge over time. The set of wrought and AM 316L plates has provided a foundational dataset of relationships between ultrasonic data and mechanical responses which will expand to new materials and geometries. Alongside the plate samples, cylindrical AM 316L samples with the same heat treatment and build parameters are available, and their NRUS testing has been completed. Early results comparing the nonlinearity parameters  $\alpha$  and  $\beta$  from NRUS and SHG show similar observable trends with mechanical strength parameters. Further work will include surface wave SHG and resonance frequency measurements on the plates and wave speed measurements on the cylinders. Microstructural characterization of these samples using electron microscopy to aid in the quantitative comparisons between microstructures and ultrasonic responses is underway. Samples of different materials and geometries will also be tested for their ultrasonic behavior, such as dog-bone Ti-6Al-4V AM samples with a variety of processing parameters.

Simulations will continue to develop in complexity and physical accuracy. After moving beyond the fundamental studies such as those presented in this research, SEM micrographs of the existing 316L and Ti-6Al-4V samples will be explicitly modeled to create a set of synthetic microstructures. These microstructure-informed models will have their mechanical and ultrasonic responses simulated. Linear wave propagation will be conducted, followed by the implementation of different constitutive models and multi-scale nonlinear wave propagation

studies intended to emulate physical testing. Systematic variations of microstructural properties in the synthetic models will result in a larger, versatile dataset for mechanical, linear, and nonlinear testing to be simulated. The hybrid dataset between simulations and experimental data will continue to grow in this manner.

The construction of a physics-informed machine learning (ML) infrastructure capable of predicting mechanical response and microstructural defects from the measured ultrasonic parameters will also be researched. The desired outcome is a generalizable model with the capability to predict the structure and properties of AM components from nondestructive ultrasonic responses. This will enable the efficient and reliable certification of AM components using ultrasonic evaluation methods.

This work and its future objectives seek to provide new information to reduce the knowledge gap on the interrelations among a material's ultrasonic response, microstructural features, and mechanical properties. The novel combination of microstructural modeling, simulations, and experimental work provide a unique opportunity to pursue an understanding of the quantitative linkage between microstructure and properties of AM materials nondestructively, with the ultimate goal of efficient and reliable AM parts qualification. The realization of these objectives in manufacturing will have an immense impact on innumerable industries including defense, biomedical, petrochemical, transportation, and more. The generalization of this framework also enables extension into other materials, such as composites, in the move towards the wider industrial adoption of additive manufacturing.

## Appendix A

### MATLAB Script for Ultrasonic Data Analysis

```
%% Script to Process Ultrasonic Data Binary Files
% Colin Williams
% This script takes a given set of ultrasonic data and info of .dat format.
% Inputs include the data and info binary files from ultrasonic testing and
several relevant variables to characterize the signal.
% Outputs include plots of data, spectra, and nonlinearity parameter.
clc;    % Clear the command window.
close all; % Close all figures
clear; % Erase all existing variables.
set(0,'defaulttextinterpreter','latex')
set(groot,'defaultAxesTickLabelInterpreter','latex');
% PLATE NUMBER
plate = 2;
% LOCATION NUMBER
location = 1;
A1 = [];
j = 1;
polyno = 4; % For the polynomial fitting of peak maxes
% Variables to Adjust (User Input)
center_freq_1 = 5e6;
center_freq_2 = 2*center_freq_1;
% For experiment
time_beg = 2.25;
```

```

time_end = 5.5;

for j = 1:20 % Set to number of amplitudes recorded
filenamedata = sprintf('AM-900-23_4_Trial7_run%d_data.dat',j);
filenameinfo = sprintf('AM-900-23_4_Trial7_run%d_info.dat',j);
    INFO = importdata(filenameinfo);
    fid = fopen(filenamedata, 'r');
    signal = fread(fid,'double');
    status = fclose(fid);

% Testing Parameters
f_s = INFO(1,2); % Sampling Frequency
recordtime = INFO(1,5);
recordtime_us = recordtime*10^6;
t_s = 1/f_s; % Time Step
N = round(recordtime/t_s); % Number of Points
time = (0:N-1)*t_s; % N should be for time of one acquisition
time_us = time*10^6; % micro seconds
signalmatrix = reshape(signal,N,[]) ; % N x 100 matrix
signal_mean = mean(signalmatrix,2); % Average of many pulsed signals
signal_mean = signal_mean - mean(signal_mean); % DC offset
hanning_w=[zeros(round((time_beg*N/recordtime_us),1); ... % Windowing
hanning(round((time_end-time_beg)*N/recordtime_us)); ...
zeros((round((recordtime_us-time_end)*N/recordtime_us)-1),1)];
signalhanning=signal_mean.*hanning_w;

figure
plot(time_us,signal_mean)
title('Signal Mean vs. Time')
xlabel('time (\mus)');

```

```

ylabel('amplitude (log scale) (V)')
set(gca,'FontName','cmr12')
set(gca,'FontSize',16);
ax = gca;
ax.YRuler.Exponent = 0;
ax.XRuler.Exponent = 0;
N=5000; % More points to improve FFT
% Resolution
df = 1/(t_s*(N-1)); % max time scale
f_nyq = f_s/2; % Nyquist Frequency
% FFT Spectrum of Data
S = fft(signalhanning,N);
abs_S = abs(S);
f_vector = 0:df:f_nyq;
half_S = abs_S(1:N/2);
% Find the amplitude of each harmonic
[xA1] = [(center_freq_1 - 0.2*center_freq_1),(center_freq_1 +
0.2*center_freq_1)]; % Input variable method
% Peak finder
[pks_1,locs_1] = findpeaks(half_S(1:750));
max_peak_1 = max(pks_1);
max_loc_1 = find(half_S == max_peak_1);
peak_find_f_vec_1 = f_vector(max_loc_1);
index_1 = [max_loc_1-5 max_loc_1+5];
[spect_value_1,index_max_1]=max(half_S(index_1(1):index_1(2)));
% Find the maximum value of the function half_S over the range
% index(1) to index(2) where 'half_S' is the spectrum

```

```

index_max_1=index_max_1+index_1(1)-1;
% converts the found index to the real position of the index in strainfilt
poly_1=polyfit(transpose(f_vector(index_max_1-
polyno:index_max_1+polyno)),half_S(index_max_1-polyno:index_max_1+polyno),2);
% fit a second order polynomial to points within (polyno) number of points of
the previously found maximum
max_pos_1 = (-poly_1(2)/(2*poly_1(1))); % equivalent to  $-b/2a$ 
better_amp_1 = polyval(poly_1,max_pos_1);
A1(j) = better_amp_1;
y1 = polyval(poly_1, f_vector);
% Amplitude 2: Picking second order frequency range
% Peak Finder 2
[pks_2,locs_2] = findpeaks(half_S(185:235));
max_peak_2 = max(pks_2);
max_loc_2 = find(half_S == max_peak_2);
peak_find_f_vec_2 = f_vector(max_loc_2);
index_2 = [max_loc_2-5 max_loc_2+5];
[spect_value_2,index_max_2]=max(half_S(index_2(1):index_2(2)));
index_max_2=index_max_2+index_2(1)-1;
poly_2=polyfit(transpose(f_vector(index_max_2-
polyno:index_max_2+polyno)),half_S(index_max_2-polyno:index_max_2+polyno),2);
max_pos_2 = (-poly_2(2)/(2*poly_2(1)));
better_amp_2 = polyval(poly_2,max_pos_2);
A2_poly(j) = better_amp_2;
y2 = polyval(poly_2, f_vector);
% Peak Finder 3
[pks_3,locs_3] = findpeaks(half_S(270:350));

```

```

max_peak_3 = max(pks_3);
max_loc_3 = find(half_S == max_peak_3);
peak_find_f_vec_3 = f_vector(max_loc_3);
index_3 = [max_loc_3-5 max_loc_3+5];
[spect_value_3,index_max_3]=max(half_S(index_3(1):index_3(2)));
index_max_3=index_max_3+index_3(1)-1;
poly_3=polyfit(transpose(f_vector(index_max_3-
polyno:index_max_3+polyno)),half_S(index_max_3-polyno:index_max_3+polyno),2);
max_pos_3 = (-poly_3(2)/(2*poly_3(1)));
better_amp_3 = polyval(poly_3,max_pos_3);
A3_poly(j) = better_amp_3; % note we dont use the poly fit for run #1 due to
error in final fitting
y3 = polyval(poly_3, f_vector);
figure
semilogy(f_vector/1e6, half_S, 'ko')
xlabel("Frequency (MHz)")
xlim([0 25])
ylabel("Amplitude (a.u)")
hold on
plot(max_pos_1/1e6,better_amp_1, 'm*')
plot(max_pos_2/1e6,better_amp_2, 'm*')
plot(max_pos_3/1e6,better_amp_3, 'm*')
hold on
legend('Signal')
set(gca, 'FontName', 'cmr12')
set(gca, 'FontSize', 20);
ax = gca;

```

```

ax.YRuler.Exponent = 0;
ax.XRuler.Exponent = 0;

end

%% The Plotting Section

A1_squared = A1.^2;

% Plot A1^2 vs A2 from each of the 20 runs using Polyfit A2

figure

plot(A1_squared,A2_poly,'o','MarkerSize', 10, 'LineWidth', 1.5)

title(['(LANL ',sprintf('%d ',plate) 'Loc ',sprintf('%d)',location) '
$$A_1^2$$ vs. $$A_2$$'])

xlabel('$$A_1^2$$')

ylabel('$$A_2$$')

set(gca,'FontName','cmr12')

set(gca,'FontSize',20);

ax = gca;

ax.YRuler.Exponent = 0;

ax.XRuler.Exponent = 0;

% Plot log10(A_1) vs log10(A_2)

figure

plot(log10(A1),log10(A2_poly),'o','MarkerSize', 10, 'LineWidth', 1.5)

xlabel('log($$A_1$$)')

ylabel('log($$A_2$$)')

set(gca,'FontName','cmr12')

set(gca,'FontSize',20);

ax = gca;

ax.YRuler.Exponent = 0;

ax.XRuler.Exponent = 0;

```

```

time_interval = linspace(1,120,60);
qq = A2_poly./A1_squared;
qq_scale = qq*10E3;
qq_norm = normalize(qq_scale, 'range');
%% Looking at different sections of log-log or A2 vs A1^2
a = 1; % Lower bound
b = 10; % Upper bound
% Next few lines find the linear slope of the plots on a specified range
logA1 = log10(A1);
logA2 = log10(A2_poly);
log_coef = polyfit(logA1(a:b),logA2(a:b),1) ;
log_slope = log_coef(1) ;
A1A2_coef = polyfit(A1_squared(a:b),A2_poly(a:b),1) ;
A1A2_slope = A1A2_coef(1) ;
A1_ExpB = A1.^(log_slope);
% Plot A1^B and A2
figure
plot(A1_ExpB,A2_poly,'o','MarkerSize', 10, 'LineWidth', 1.5)
title(['(LANL ',sprintf('%d ',plate) 'Loc ',sprintf('%d)',location) ' '$A_1$$
B vs. '$A_2$$'])
xlabel(''$A_1 B$$')
ylabel(''$A_2$$')
set(gca,'FontName','cmr12')
set(gca,'FontSize',20);
ax = gca;
ax.YRuler.Exponent = 0;
ax.XRuler.Exponent = 0;

```

```
% Save Vectors to File in This Folder  
save('AM-900-23_4_T7_A2', 'A2_poly')  
save('AM-900-23_4_T7_A1^2', 'A1_squared')
```

## Appendix B

### Python Script for ABAQUS Simulations

```

# Python Script to Generate 2D Plate w/ randomly distributed hets
# Created by Colin Williams
# This version does not yet run the simulation on its own.

from abaqus import *
from abaqusConstants import *
import __main__
import section
import regionToolset
import displayGroupMdbToolset as dgm
import part
import material
import assembly
import step
import interaction
import load
import mesh
import optimization
import job
import sketch
import visualization
import xyPlot
import displayGroupOdbToolset as dgo
import connectorBehavior
import numpy as np
import random

# User input plate geometry and porosity parameters -----

# Geometry
H = 0.01 # meters
W = 0.01
h=H*0.975 #Inner Height
w=W*0.975 #Inner Width
dh=0
receiver_size = 3e-3 # Size of node set making the receiver

X=np.array([0,W,W,0,0])
Y=np.array([0,0,H,H,0])

# Simulation Time Parameters
step_time = 6E-6 # Length of TOTAL simulation
time_step = 4e-9 # Time step for running sim = 1/sampling_freq

q=1

# Wave Parameters
wave_amp = 1e-6 # For displacement BC

```

```

Frequency = 5E6 # Hz
Wave_Velo = 5850 # m/s
Lambda = Wave_Velo/Frequency
Elem_per_Lambda = 25
devFactor = 0.07 # Mesh size deviation factor

# Porosity Parameters
rmin=90e-6
rmax=90e-6
porositymin=0.2
porositymax=0.2

Node_Tol = 1

# Check to make sure heterogeneities do not intersect border of plate
def CheckBorder(x,y,r,W,H):
    """
    dist=np.array([x,y,W-x,H-y])
    gamma=0.2
    if dist.min()<r*(1+gamma):
        A=False
    else:
        A=True

    return A;

def CheckOverlap(x,y,r,xi,yi,ri):
    """
    nc=len(xi)
    gamma=2
    B=True

    for i in range(0,nc):
        if np.sqrt((x-xi[i])**2+(y-yi[i])**2)<r+ri[i]+gamma*r:
            B=False
            break

    return B;
# Create porosity/heterogeneities -----

porosity=porositymin+(porositymax-porositymin)*random.random()
totalarea=(H+dh)*(W)
populatedarea=0
ic=0
ri=np.array([])
xi=np.array([])
yi=np.array([])
for i in range(0,10000):
    xmin=rmin
    ymin=rmin
    xmax=w-rmin
    ymax=h-rmin

```

```

r=rmin+(rmax-rmin)*random.random()
x=xmin+(xmax-xmin)*random.random()
y=ymin+(ymax-ymin)*random.random()

A=CheckBorder(x,y,r,w,h)

if A==True:
    if ic==0:
        ic=1
        B=True
    else:
        B=CheckOverlap(x,y,r,xi,yi,ri)
        if B==True:
            ic=ic+1
            if A and B == True:
                if populatedarea<=h*w:
                    if (populatedarea+np.pi*r**2)/totalarea<=porosity:
                        populatedarea=populatedarea+np.pi*r**2
                        ri=np.append(ri,r)
                        xi=np.append(xi,x)
                        yi=np.append(yi,y)

xi=xi+(W-w)/2
yi=yi+(H-h)/2+dh/2

# Create Parts -----
mdb.Model(name='Model-%d' %(q), modelType=STANDARD_EXPLICIT)
mdb.models['Model-%d' %(q)].ConstrainedSketch(name='__profile__',
sheetSize=W)

# Create Plate/Matrix -----

mdb.models['Model-%d' %(q)].ConstrainedSketch(name='__profile__',
sheetSize=W)
mdb.models['Model-
1'].sketches['__profile__'].rectangle(point1=(0,0),point2=(W,H))
mdb.models['Model-%d' %(q)].Part ( dimensionality = TWO_D_PLANAR , name
='Plate'
, type =
DEFORMABLE_BODY)
mdb.models['Model-%d' %(q)].parts ['Plate'].BaseShell(sketch =
mdb.models['Model-%d' %(q)].sketches['__profile__'])
del mdb.models['Model-%d' %(q)].sketches['__profile__']

# Assembly -----

a = mdb.models['Model-%d' %(q)].rootAssembly
p = mdb.models['Model-%d' %(q)].parts['Plate']
a.Instance(name='Plate-1', part=p, dependent=OFF)

# Assign the Material Properties -----

```

```

E_Bulk=210.38e9 # Bulk Material
vv_Bulk=0.277
density_Bulk=7800

mdb.models['Model-%d' % (q)].Material(name='Bulk')
mdb.models['Model-%d' % (q)].materials['Bulk'].Elastic(table=((E_Bulk,
vv_Bulk), ))
mdb.models['Model-%d' % (q)].materials['Bulk'].Density(table=((density_Bulk, )
, ))

# Create Sections-----

mdb.models['Model-%d' % (q)].HomogeneousSolidSection(name='Bulk_Section',
material='Bulk', thickness=None)

# Assign -----

faces = mdb.models['Model-%d' % (q)].parts['Plate'].faces
region = regionToolset.Region(faces=faces)
mdb.models['Model-%d' % (q)].parts['Plate'].SectionAssignment(region=region,
sectionName='Bulk_Section', offset=0.0,
offsetType=MIDDLE_SURFACE, offsetField='',
thicknessAssignment=FROM_SECTION)

# Create Step for Wave Prop -----

mdb.models['Model-%d' % (q)].ExplicitDynamicsStep(name='Wave_Prop',
previous='Initial', timePeriod=step_time, improvedDtMethod=ON)

# Seed the edges and establish node pairs -----

a = mdb.models['Model-%d' % (q)].rootAssembly
e = a.instances['Plate-1'].edges

EdgeUp = e.findAt((W/2.0,H,0.0))
EdgeDo = e.findAt((W/2.0,0.0,0.0))
EdgeRi = e.findAt((W,H/2.0,0.0))
EdgeLe = e.findAt((0.0,H/2.0,0.0))

q1 = EdgeUp.index
q2 = EdgeDo.index
q3 = EdgeRi.index
q4 = EdgeLe.index

EdUp = e[q1:q1+1]
EdDo = e[q2:q2+1]
EdRi = e[q3:q3+1]
EdLe = e[q4:q4+1]

a.Set(edges=EdUp, name = 'Up')
a.Set(edges=EdDo, name = 'Down')
a.Set(edges=EdRi, name = 'Right')
a.Set(edges=EdLe, name = 'Left')

```

### # Local Seed on Edges

```
EdgeMeshSize = Lambda/Elem_per_Lambda
```

```
NumMeshRi = int(H/EdgeMeshSize)
```

```
NumMeshUp = int(W/EdgeMeshSize)
```

```
a = mdb.models['Model-%d' % (q)].rootAssembly
```

```
p = a.instances['Plate-1']
```

```
a.seedEdgeByNumber(edges=EdRi, number = NumMeshRi, constraint = FIXED)
```

```
a.seedEdgeByNumber(edges=EdLe, number = NumMeshRi, constraint = FIXED)
```

```
a.seedEdgeByNumber(edges=EdUp, number = NumMeshUp, constraint = FIXED)
```

```
a.seedEdgeByNumber(edges=EdDo, number = NumMeshUp, constraint = FIXED)
```

### # Apply Global Seed

```
a = mdb.models['Model-%d' % (q)].rootAssembly
```

```
partInstances = (a.instances['Plate-1'], )
```

```
a.seedPartInstance(regions = partInstances, size = EdgeMeshSize,
deviationFactor=0.1, minSizeFactor=0.1)
```

```
elemType1 = mesh.ElemType(elemCode=CPE4R, elemLibrary=STANDARD,
```

```
secondOrderAccuracy=OFF, hourglassControl=DEFAULT, distortionControl=DEFAULT)
```

```
elemType2 = mesh.ElemType(elemCode=CPE3, elemLibrary=STANDARD)
```

```
a = mdb.models['Model-%d' % (q)].rootAssembly
```

```
f = a.instances['Plate-1'].faces
```

```
pickedRegions = (f,)
```

```
a.setElementType(regions=pickedRegions, elemTypes=(elemType1,elemType2))
```

```
a.generateMesh(regions=partInstances) # Mesh Part
```

### # Finding the Faces in the Plate

### # Storing Nodes of Faces for PBC

```
Upnodes = a.sets['Up'].nodes
```

```
Downnodes = a.sets['Down'].nodes
```

```
Rightnodes = a.sets['Right'].nodes
```

```
Leftnodes = a.sets['Left'].nodes
```

### # Storing coordinates and labels of face nodes

```
UpCoord = []
```

```
DownCoord = []
```

```
RightCoord = []
```

```
LeftCoord = []
```

```
for node in Upnodes:
```

```
    UpCoord = UpCoord +
```

```
    [[node.coordinates[0],node.coordinates[1],node.label]]
```

```

for node in Downnodes:
    DownCoord = DownCoord +
    [[node.coordinates[0],node.coordinates[1],node.label]]

for node in Rightnodes:
    RightCoord = RightCoord +
    [[node.coordinates[0],node.coordinates[1],node.label]]

for node in Leftnodes:
    LeftCoord = LeftCoord +
    [[node.coordinates[0],node.coordinates[1],node.label]]

UpCoord.sort()
DownCoord.sort()
RightCoord.sort()
LeftCoord.sort()

# Create sets for the top and bottom (up or down) edges

NumUp = len(UpCoord)

for i in range(0,NumUp):

    if (abs(UpCoord[i][0]-DownCoord[i][0])<Node_Tol):
        NLabel = DownCoord[i][2]
        a.Set(nodes=p.nodes[NLabel-1:NLabel], name = 'DownNode_'+str(i))
        NLabel = UpCoord[i][2]
        a.Set(nodes=p.nodes[NLabel-1:NLabel], name = 'UpNode_'+str(i))

    else:
        print 'Distance between the nodes is greater than tolerance.'

# Create sets for the left and right edges

NumRi = len(RightCoord)

for i in range(0,NumRi):

    if (abs(RightCoord[i][1]-LeftCoord[i][1])<Node_Tol):
        NLabel = RightCoord[i][2]
        a.Set(nodes=p.nodes[NLabel-1:NLabel], name='RightNode_'+str(i))
        NLabel = LeftCoord[i][2]
        a.Set(nodes=p.nodes[NLabel-1:NLabel], name='LeftNode_'+str(i))

    else:
        print 'Distance between the nodes is greater than tolerance.'

# Define the Periodic Constraints Up and Down

for i in range(1,NumUp):
    mdb.models['Model-%d' %q].Equation(name='Const-UpDown-y'+str(i),
    terms=((1.0,
            'DownNode_'+str(i), 2), (1.0, 'UpNode_'+str(i), 2), (1.0,

```

```

        'UpNode_0', 2)))

for i in range(1, NumUp):
    mdb.models['Model-%d' % (q)].Equation(name='Const-UpDown-x'+str(i),
    terms=((1.0,
            'DownNode_'+str(i), 1), (1.0, 'UpNode_'+str(i), 1)))

# Pin the bottom left corner in the x and y directions

a = mdb.models['Model-%d' % (q)].rootAssembly
v = a.instances['Plate-1'].vertices

ver = v.findAt((0,0,0))
q1 = ver.index
Fixver = v[q1:q1+1]
region = a.Set(vertices = Fixver, name = 'Set-Fix')
mdb.models['Model-%d' % (q)].DisplacementBC(name = 'Fix', createStepName=
'Initial',
    region=region, u1=0, u2=0, ur3=UNSET, amplitude=UNSET,
    fixed=OFF, distributionType=UNIFORM, fieldName='', localCsys=None)

# Pin the top left corner along the x direction
a = mdb.models['Model-%d' % (q)].rootAssembly
v = a.instances['Plate-1'].vertices

ver = v.findAt((0,H,0))
q1 = ver.index
Movever = v[q1:q1+1]
region = a.Set(vertices = Movever, name = 'LeftX')
mdb.models['Model-%d' % (q)].DisplacementBC(name = 'LeftX', createStepName=
'Initial',
    region=region, u1=0, u2=UNSET, ur3=UNSET, amplitude=UNSET,
    fixed=OFF, distributionType=UNIFORM, fieldName='', localCsys=None)

# Pin the bottom right corner along the x direction
a = mdb.models['Model-%d' % (q)].rootAssembly
v = a.instances['Plate-1'].vertices
ver = v.findAt((W,0,0))
q1 = ver.index
Movever = v[q1:q1+1]
region = a.Set(vertices = Movever, name = 'RightX')
mdb.models['Model-%d' % (q)].DisplacementBC(name = 'RightX', createStepName=
'Initial',
    region=region, u1=UNSET, u2=0, ur3=UNSET, amplitude=UNSET,
    fixed=OFF, distributionType=UNIFORM, fieldName='', localCsys=None)

# Create an amplitude for the 5MHZ wave from existing data

mdb.models['Model-%d' % (q)].TabularAmplitude(name='FiveMHZ', timeSpan=STEP,
    smooth=SOLVER_DEFAULT, data=

# Create a displacement BC for wave prop

```

```
a = mdb.models['Model-%d' % (q)].rootAssembly
region = a.sets['LeftNode_43']
mdb.models['Model-%d' % (q)].DisplacementBC(name='WaveProp',
createStepName='Wave_Prop', region=region, u1=1e-08, u2=UNSET, ur3=UNSET,
amplitude='FiveMHZ', fixed=OFF, distributionType=UNIFORM, fieldName='',
localCsys=None)
```

## References

- [1] “DoD Additive Manufacturing Strategy,” *America Makes*, Jan. 25, 2021. <https://www.americamakes.us/dod-additive-manufacturing-strategy/> (accessed Oct. 14, 2021).
- [2] S. Van Bael, G. Kerckhofs, M. Moesen, G. Pyka, J. Schrooten, and J. P. Kruth, “Micro-CT-based improvement of geometrical and mechanical controllability of selective laser melted Ti6Al4V porous structures,” *Mater. Sci. Eng. A*, vol. 528, no. 24, pp. 7423–7431, Sep. 2011, doi: 10.1016/j.msea.2011.06.045.
- [3] G. Pyka, G. Kerckhofs, I. Papantoniou, M. Speirs, J. Schrooten, and M. Wevers, “Surface Roughness and Morphology Customization of Additive Manufactured Open Porous Ti6Al4V Structures,” *Materials*, vol. 6, no. 10, Art. no. 10, Oct. 2013, doi: 10.3390/ma6104737.
- [4] M. Seifi *et al.*, “Progress Towards Metal Additive Manufacturing Standardization to Support Qualification and Certification,” *JOM*, vol. 69, no. 3, pp. 439–455, Mar. 2017, doi: 10.1007/s11837-017-2265-2.
- [5] S. A. M. Tofail, E. P. Koumoulos, A. Bandyopadhyay, S. Bose, L. O’Donoghue, and C. Charitidis, “Additive manufacturing: scientific and technological challenges, market uptake and opportunities,” *Mater. Today*, vol. 21, no. 1, pp. 22–37, Jan. 2018, doi: 10.1016/j.mattod.2017.07.001.
- [6] P. Nanekar and B. Shah, “Characterization of material properties by ultrasonic,” *BARC Newsl*, vol. 249, Jan. 2003.
- [7] P. Khalili and P. Cawley, “The choice of ultrasonic inspection method for the detection of corrosion at inaccessible locations,” *NDT E Int.*, vol. 99, pp. 80–92, Oct. 2018, doi: 10.1016/j.ndteint.2018.06.003.
- [8] A. Khalid *et al.*, “Assessment and Characterization of Welded Mild Steel (E-6013) Using Ultrasonic Testing and Hilbert Huang Transform,” *Russ. J. Nondestruct. Test.*, vol. 57, no. 5, pp. 401–407, May 2021, doi: 10.1134/S106183092105003X.
- [9] A. A. Shah, Y. Ribakov, and Ch. Zhang, “Efficiency and sensitivity of linear and non-linear ultrasonics to identifying micro and macro-scale defects in concrete,” *Mater. Des.*, vol. 50, pp. 905–916, Sep. 2013, doi: 10.1016/j.matdes.2013.03.079.
- [10] A. N. Sinclair and H. Eng, “Ultrasonic Determination of Fracture Toughness,” in *Nondestructive Characterization of Materials II*, J. F. Bussière, J.-P. Monchalain, C. O. Ruud, and R. E. Green, Eds. Boston, MA: Springer US, 1987, pp. 251–259. doi: 10.1007/978-1-4684-5338-6\_24.
- [11] K. H. Matlack, J.-Y. Kim, L. J. Jacobs, and J. Qu, “Review of Second Harmonic Generation Measurement Techniques for Material State Determination in Metals,” *J. Nondestruct. Eval.*, vol. 34, no. 1, p. 273, Nov. 2014, doi: 10.1007/s10921-014-0273-5.
- [12] W. J. N. de Lima and M. F. Hamilton, “Finite-amplitude waves in isotropic elastic plates,” *J. Sound Vib.*, vol. 265, no. 4, pp. 819–839, Aug. 2003, doi: 10.1016/S0022-460X(02)01260-9.
- [13] S.-H. Park, J. Kim, D.-G. Song, S. Choi, and K.-Y. Jhang, “Measurement of Absolute Acoustic Nonlinearity Parameter Using Laser-Ultrasonic Detection,” *Appl. Sci.*, vol. 11, no. 9, Art. no. 9, Jan. 2021, doi: 10.3390/app11094175.
- [14] W. T. Yost, J. H. Cantrell, and M. A. Breazeale, “Ultrasonic nonlinearity parameters and third-order elastic constants of copper between 300 and 3 °K,” *J. Appl. Phys.*, vol. 52, no. 1, pp. 126–128, Jan. 1981, doi: 10.1063/1.328443.
- [15] M. Climent, M. Miró, J. Carbajo, P. Poveda Martínez, G. Vera, and J. Soriano, “Use of Non-Linear Ultrasonic Techniques to Detect Cracks Due to Steel Corrosion in Reinforced Concrete Structures,” *Materials*, vol. 12, p. 813, Mar. 2019, doi: 10.3390/ma12050813.
- [16] S. Zhang, X. Li, C. Chen, H. Jeong, and G. Xu, “Characterization of Aging Treated 6061 Aluminum Alloy Using Nonlinear Rayleigh Wave,” *J. Nondestruct. Eval.*, vol. 38, no. 4, p. 88, Sep. 2019, doi: 10.1007/s10921-019-0630-5.

- [17] M. Liu, J.-Y. Kim, L. Jacobs, and J. Qu, “Experimental study of nonlinear Rayleigh wave propagation in shot-peened aluminum plates—Feasibility of measuring residual stress,” *NDT E Int.*, vol. 44, no. 1, pp. 67–74, Jan. 2011, doi: 10.1016/j.ndteint.2010.09.008.
- [18] H. Jeong, S.-H. Nahm, K.-Y. Jhang, and Y.-H. Nam, “A nondestructive method for estimation of the fracture toughness of CrMoV rotor steels based on ultrasonic nonlinearity,” *Ultrasonics*, vol. 41, no. 7, pp. 543–549, Sep. 2003, doi: 10.1016/S0041-624X(03)00154-9.
- [19] C. Williams, C. Borigo, J. Rivière, C. J. Lissenden, and P. Shokouhi, “Nondestructive Evaluation of Fracture Toughness in 4130 Steel Using Nonlinear Ultrasonic Testing,” *J. Nondestruct. Eval.*, vol. 41, no. 1, p. 13, Jan. 2022, doi: 10.1007/s10921-022-00846-5.
- [20] S. Maier, J.-Y. Kim, M. Forstehäusler, J. J. Wall, and L. J. Jacobs, “Noncontact nonlinear resonance ultrasound spectroscopy (NRUS) for small metallic specimens,” *NDT E Int.*, vol. 98, pp. 37–44, Sep. 2018, doi: 10.1016/j.ndteint.2018.04.003.
- [21] S. K. Chakrapani and D. J. Barnard, “Determination of acoustic nonlinearity parameter ( $\beta$ ) using nonlinear resonance ultrasound spectroscopy: Theory and experiment,” *J. Acoust. Soc. Am.*, vol. 141, no. 2, pp. 919–928, Feb. 2017, doi: 10.1121/1.4976057.
- [22] N. Kamali, N. Tehrani, A. Mostavi, S.-W. Chi, D. Ozevin, and J. E. Indacochea, “Influence of Mesoscale and Macroscale Heterogeneities in Metals on Higher Harmonics Under Plastic Deformation,” *J. Nondestruct. Eval.*, vol. 38, no. 2, p. 53, Apr. 2019, doi: 10.1007/s10921-019-0593-6.
- [23] N. Kamali, A. Mahdavi, and S.-W. Chi, “Numerical study on how heterogeneity affects ultrasound high harmonics generation,” *Nondestruct. Test. Eval.*, vol. 35, no. 2, pp. 158–176, Jun. 2020, doi: 10.1080/10589759.2019.1652295.
- [24] A. Van Pamel, C. R. Brett, P. Huthwaite, and M. J. S. Lowe, “Finite element modelling of elastic wave scattering within a polycrystalline material in two and three dimensions,” *J. Acoust. Soc. Am.*, vol. 138, no. 4, pp. 2326–2336, Oct. 2015, doi: 10.1121/1.4931445.
- [25] A. Van Pamel, G. Sha, S. I. Rokhlin, and M. J. S. Lowe, “Finite-element modelling of elastic wave propagation and scattering within heterogeneous media,” *Proc. R. Soc. Math. Phys. Eng. Sci.*, vol. 473, no. 2197, p. 20160738, Jan. 2017, doi: 10.1098/rspa.2016.0738.
- [26] A. Hikata, B. B. Chick, and C. Elbaum, “Dislocation Contribution to the Second Harmonic Generation of Ultrasonic Waves,” *J. Appl. Phys.*, vol. 36, no. 1, pp. 229–236, Jan. 1965, doi: 10.1063/1.1713881.
- [27] Y. Li, S. Hu, and C. H. Henager, “Microstructure-based model of nonlinear ultrasonic response in materials with distributed defects,” *J. Appl. Phys.*, vol. 125, no. 14, p. 145108, Apr. 2019, doi: 10.1063/1.5083957.
- [28] B. Fuchs *et al.*, “Analytical modeling of the evolution of the nonlinearity parameter of sensitized stainless steel,” *J. Appl. Phys.*, vol. 130, no. 16, p. 165102, Oct. 2021, doi: 10.1063/5.0053632.
- [29] R. Qiao and X. Yan, “The Characterization of Fatigue Damage of 316L Stainless Steel Parts Formed by Selective Laser Melting with Harmonic Generation Technique,” *Materials*, vol. 15, no. 3, Art. no. 3, Jan. 2022, doi: 10.3390/ma15030718.
- [30] A. Bellotti, J.-Y. Kim, J. E. Bishop, B. H. Jared, D. Susan, and L. J. Jacobs, “Nonlinear ultrasonic technique for the quantification of dislocation density in additive materials,” *AIP Conf. Proc.*, vol. 2102, no. 1, p. 020040, May 2019, doi: 10.1063/1.5099744.
- [31] A. Bellotti *et al.*, “Nonlinear ultrasonic technique for the characterization of microstructure in additive materials,” *J. Acoust. Soc. Am.*, vol. 149, no. 1, pp. 158–166, Jan. 2021, doi: 10.1121/10.0002960.
- [32] J. Kober *et al.*, “Assessing Porosity in Selective Electron Beam Melting Manufactured Ti–6Al–4V by Nonlinear Impact Modulation Spectroscopy,” *J. Nondestruct. Eval.*, vol. 39, no. 4, p. 86, Nov. 2020, doi: 10.1007/s10921-020-00731-z.

- [33] E. Bozek, S. McGuigan, Z. Snow, E. W. Reutzel, J. Rivière, and P. Shokouhi, “Nonlinear resonance ultrasonic spectroscopy (NRUS) for the quality control of additively manufactured samples,” *NDT E Int.*, vol. 123, p. 102495, Oct. 2021, doi: 10.1016/j.ndteint.2021.102495.
- [34] J. A. Slotwinski, E. J. Garboczi, and K. M. Hebenstreit, “Porosity Measurements and Analysis for Metal Additive Manufacturing Process Control,” *J. Res. Natl. Inst. Stand. Technol.*, vol. 119, pp. 494–528, Sep. 2014, doi: 10.6028/jres.119.019.
- [35] R. Song, J. Xiang, and D. Hou, “Characteristics of Mechanical Properties and Microstructure for 316L Austenitic Stainless Steel,” *J. Iron Steel Res. Int.*, vol. 18, no. 11, pp. 53–59, Nov. 2011, doi: 10.1016/S1006-706X(11)60117-9.
- [36] K. Rokosz, J. Lahtinen, T. Hryniewicz, and S. Rzakiewicz, “XPS depth profiling analysis of passive surface layers formed on austenitic AISI 304L and AISI 316L SS after high-current-density electropolishing,” *Surf. Coat. Technol.*, vol. 276, pp. 516–520, Aug. 2015, doi: 10.1016/j.surfcoat.2015.06.022.
- [37] J. H. Lee and Y. Kim, “Intergranular Corrosion of 316L Stainless Steel by Aging and UNSM (Ultrasonic Nano-crystal Surface Modification) treatment,” *Corros. Sci. Technol.*, vol. 14, pp. 313–324, Dec. 2015, doi: 10.14773/cst.2015.14.6.313.
- [38] Zitelli, Folgarait, and Di Schino, “Laser Powder Bed Fusion of Stainless Steel Grades: A Review,” *Metals*, vol. 9, no. 7, p. 731, Jun. 2019, doi: 10.3390/met9070731.
- [39] D. Torello, S. Thiele, K. H. Matlack, J.-Y. Kim, J. Qu, and L. J. Jacobs, “Diffraction, attenuation, and source corrections for nonlinear Rayleigh wave ultrasonic measurements,” *Ultrasonics*, vol. 56, pp. 417–426, Feb. 2015, doi: 10.1016/j.ultras.2014.09.008.
- [40] J. H. Cantrell and X.-G. Zhang, “Nonlinear acoustic response from precipitate-matrix misfit in a dislocation network,” *J. Appl. Phys.*, vol. 84, no. 10, pp. 5469–5472, Nov. 1998, doi: 10.1063/1.368309.
- [41] M. S. Pham, B. Dovggy, and P. A. Hooper, “Twinning induced plasticity in austenitic stainless steel 316L made by additive manufacturing,” *Mater. Sci. Eng. A*, vol. 704, pp. 102–111, Sep. 2017, doi: 10.1016/j.msea.2017.07.082.
- [42] L. Ladani and M. Sadeghilaridjani, “Review of Powder Bed Fusion Additive Manufacturing for Metals,” *Metals*, vol. 11, no. 9, Art. no. 9, Sep. 2021, doi: 10.3390/met11091391.
- [43] T. Ronneberg, C. M. Davies, and P. A. Hooper, “Revealing relationships between porosity, microstructure and mechanical properties of laser powder bed fusion 316L stainless steel through heat treatment,” *Mater. Des.*, vol. 189, p. 108481, Apr. 2020, doi: 10.1016/j.matdes.2020.108481.
- [44] A. du Plessis, I. Yadroitsava, and I. Yadroitsev, “Effects of defects on mechanical properties in metal additive manufacturing: A review focusing on X-ray tomography insights,” *Mater. Des.*, vol. 187, p. 108385, Feb. 2020, doi: 10.1016/j.matdes.2019.108385.
- [45] J. Kim and K.-Y. Jhang, “Evaluation of Ultrasonic Nonlinear Characteristics in Heat-Treated Aluminum Alloy (Al-Mg-Si-Cu),” *Adv. Mater. Sci. Eng.*, vol. 2013, p. e407846, Nov. 2013, doi: 10.1155/2013/407846.
- [46] M. Jaskari, S. Ghosh, I. Miettunen, P. Karjalainen, and A. Järvenpää, “Tensile Properties and Deformation of AISI 316L Additively Manufactured with Various Energy Densities,” *Materials*, vol. 14, no. 19, Art. no. 19, Jan. 2021, doi: 10.3390/ma14195809.